Band structure of monolayer transition-metal dichalcogenides and topological properties of their nanoribbons: Next-nearest-neighbor hopping

A. C. Dias,[1] Fanyao Qu,[1,*] David L. Azevedo,[1] and Jiyong Fu[1,2]

[1]*Instituto de Física, Universidade de Brasília, Brasília-DF 70919-970, Brazil*
[2]*Department of Physics, Qufu Normal University, Qufu, Shandong, 273165, China*

Tight-binding (TB) models exploited in calculating band structure of monolayer transition-metal dichalcogenides (TMDCs), namely MX_2 (M = Mo and W; X = S, Se and Te), can be divided into two groups: one is based on group theory and the other uses Slater-Koster (SK) method. The former in general is lack of flexibility to be extended to *confined* finite systems with lower symmetry, e.g., nanoribbons (NRs) and quantum dots. Unlike ubiquitous TB models, here we present an improved scheme of the flexible SK TB method in which the second-nearest-neighbor M-M and X-X hopping terms are included. Its improvement, being of comparable accuracy to first-principles calculations, is clearly elucidated through a comprehensive comparison between our results and those produced by widely accepted TB models in literature for monolayer MoS_2. Besides, its high flexibility allows us to successfully extend our TB model from monolayer TMDCs to the MoX_2 (X = S, Se, and Te) and WX_2 (X = S and Se) NRs of both zigzag and armchair types. We find that the zigzag NR could be either metallic or semiconducting, depending on the spin-orbit strength and band gap of its parent two-dimensional bulk TMDC, which is in contradiction to the usual consensus concerning TMDC NRs which exhibit the metallic behavior only. For a certain Fermi level, remarkably, we discovered that the MoS_2 NRs demonstrate quantum valley Hall effect, while others only present topological insulator phase.

I. INTRODUCTION

Monolayer transition-metal dichalcogenides (TMDCs) denoted by MX_2 (M = Mo, W; X = S, Se, Te) have attracted enormous attention following the discovery of a direct band gap at the two inequivalent K and K' valleys in the visible frequency range [1–3] and the coupling of spin and valley degrees of freedom [4–7] due to lattice inversion asymmetry along with strong spin-orbit coupling (SOC) [3]. This leads to pumping light-helicity-dependent valley (and spin) selective optical transitions [3,4,8–11], and further allows for optical generation of valley polarization (optical orientation) [8,12,13], valley Hall effect [2,6], valley coherence [9,14–16], and optical manipulation of valley pseudospin [17], which makes the TMDCs promising candidates for electronic, optoelectronic, spintronic, and valleytronic applications.

In recent years, both expensive first-principles calculations on electronic structure, also called density functional theory (DFT), and simple tight-binding (TB) model have been widely used in the study of electronic structure of molecules and solids [1,18–25]. In comparison with the former, the TB model is typically two to three orders of magnitude faster. Therefore, it is particularly useful for the finite systems which possess low geometric symmetry such as quantum dots, nanoribbons (NRs), disordered and inhomogeneous samples, strained and/or bent systems, and twisted multilayer materials, in which quantum mechanical effects are significant, but the sheer number of atoms in the system makes *ab initio* calculations impractical.

For the nanostructured materials composed of the TMDCs, the situation becomes even more critical. Because the conduction and valence bands present a very rich orbital contribution, they are made by hybridization of the d orbitals of the transition-metal atom M, and the p orbitals of the chalcogen atom X, which makes the first-principles simulation much more challenging [22–25]. On the other hand, physically transparent Hamiltonian matrices of the TB model constructed by means of atomic orbitals lead to an intuitive interpretation for the electronic structure of complex systems. Hence, the TB calculation can afford the results with underlying physics more transparent than that of DFT. Another advantage of a TB description in comparison with first-principles simulation is that it provides a simple starting point for the further inclusion of many-body electron-electron interaction and of the dynamical effects of the electron-lattice interaction. Therefore, to explore physical properties of the TMDCs, the TB model is highly demanded. On the other hand, as known, owing to the two-dimensional (2D) spatial confinement and reduced dielectric screening as well as large electron and hole effective masses, the TMDCs exhibit exceptionally strong Coulomb interactions, which favor the formation of excitonic quasiparticles, e.g., excitons, trions, biexcitons, bound excitons, bound trions, etc. Interestingly, some of them can exist even at room temperature. To understand the excitonic behaviors stemmed from these quasiparticles, and valley (locked with spin) dynamics, extensive experimental studies, including photoluminescence (PL), time-resolved PL, Raman spectroscopy, ultrafast transient absorption spectroscopy, and time-resolved Kerr rotation, have been performed. Although a lot of experimental data have been reported, understanding of the underlying mechanism

---

*fanyao@unb.br

of excitonic emissions and valley dynamics is still restricted to the context of qualitative analysis due to lacking of a comprehensive microscopic theory. As mentioned previously, the outcome of TB calculation can act as starting point for developing microscopic many-body theory. Hence, in this context, the reliable TB model is also highly expected.

According to the way used to define hopping parameters, the existing TB models in literature can be roughly classified into two groups: one in which hopping parameters were defined using group theory [1,21,24] and the other where Slater-Koster (SK) two-center approximation [20,22,23,25–27] was utilized. The former can give good fit to the results of DFT simulation, but a large number of parameters are required. In addition, orbital asymmetry [28] restrains the validity of this kind of TB model to be applied to nanostructured materials due to their finite sizes such as quantum dots and NRs, even though it may work for strained bulk systems [29]. In stark contrast, the latter can straightforwardly be extended to the systems with lower geometric symmetry without relevant limitations [22]. However, it does not provide reliable results for overall band structure. Then, the developed TB models to date have been limited either by accuracy or by lack of flexibility to be extended to the heterostructured 2D systems. These urge us to develop a TB model, taking into account the second-nearest-neighbor M-M and X-X hoppings, which can make up for these deficiencies.

On the other hand, the controlled fabrication of desirable nanostructures such as TMDC NRs by means of either bottom-up or top-down approaches have been achieved [30–32]. However, except for MoS$_2$ NRs, no conclusive theoretical study about the electronic structure, especially, the topological properties of edge modes of the TMDC NRs, has been performed. One of our goals is to reveal the topological features of the TMDC NRs, including MoX$_2$ (X = S, Se, and Te) and WX$_2$ (X = S and Se) NRs.

This paper is organized as follows. In Sec. II, we first present our improved 11-band TB model for monolayer TMDCs without/with SOC. Then, we discuss our DFT calculation and
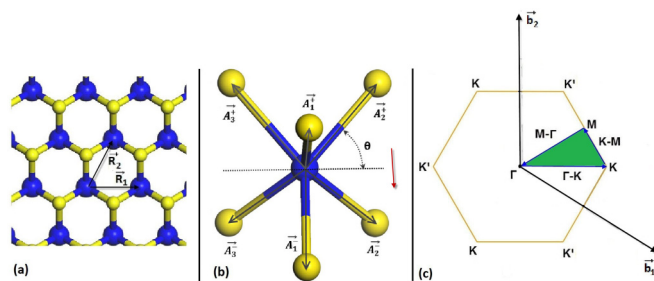
TABLE I. Lattice constant and angle θ between M-X bond and the M plane used in our calculations [33,35,36], as shown in Fig. 1(b).

	MoS$_2$	MoSe$_2$	MoTe$_2$	WS$_2$	WSe$_2$
a (Å)	3.166	3.288	3.519	3.1532	3.282
θ (rad)	0.710	0.710	0.710	0.710	0.710

extend our TB model to zigzag NRs. Finally, we construct the TB model for armchair NRs. In Sec. III, we show our main results and give our discussion. A comparison between the result of the DFT and that obtained by widely used eight TB models in literature for monolayer MoS$_2$ is given. The advantages and drawbacks are analyzed for each of these models, focusing on accuracy of its outcome and flexibility of the model. We predict the band structures of the monolayer MX_2 and show how the SOC manifests itself in the band structures. We also demonstrate the quantum valley Hall effect in MoS$_2$ NRs and topological insulator phases in other NRs. The effects of chemical composition of the NRs on edge modes are addressed. In Sec. IV, we summarize our main conclusion and give our remarks. In Appendices A–D, we show our detailed TB matrix elements.

II. SLATER-KOSTER TB MODEL FOR TMDCS

A. Crystal structure of monolayer TMDCs

A single-layer TMDC is composed of an inner layer of metal M atoms ordered on a triangular lattice, which is sandwiched between two layers of chalcogen X atoms located on the triangular lattice of alternating hollow sites in a triangular prismatic fashion. The X-M-X layers are bonded together by weak van der Waals forces. Top view of monolayer transition-metal dichalcogenides MX_2 is shown in Fig. 1(a). The triangular Bravais lattice is spanned by the basis vectors

$$\vec{R}_1 = (a, 0, 0), \quad \vec{R}_2 = \left(\frac{a}{2}, \frac{\sqrt{3}}{2}a, 0\right),$$

where a is lattice constant. The coordinates of the nearest neighbors of a Mo atom are displayed in Fig. 1(b), where θ is the angle between M-X bond and the M plane. The experimental values of both a and θ are given in Table I [33–36]. The reciprocal lattice, which is defined with respect to the triangular Bravais lattice, is depicted in Fig. 1(c). It is spanned by the vectors

$$\vec{b}_1 = \frac{4\pi}{\sqrt{3}a}\left(\frac{\sqrt{3}}{2}, -\frac{1}{2}, 0\right), \quad \vec{b}_2 = \frac{4\pi}{\sqrt{3}a}(0, 1, 0).$$

The first Brillouin zone of the TMDC is hexagonal, and the high-symmetry points Γ, K, and M are defined as follows: $\Gamma = (0, 0)$, $K = (\frac{4\pi}{3a}, 0)$, and $M = (\frac{\pi}{a}, \frac{\sqrt{3}\pi}{3a})$.

The outermost shells of the Mo and S atoms are $4d$ and $3p$ orbitals, respectively. The subbands near the top of the valence bands and the bottom of the conduction bands are predominantly contributed by d_{z^2}, d_{xy}, $d_{x^2-y^2}$. Nevertheless, the d_{xz}, d_{yz} orbitals of molybdenum, and the p_x, p_y, p_z orbitals of sulfide, as well as other inner orbitals are generally found in the subbands with higher energy. This means that

FIG. 1. (a) Top view of monolayer transition-metal dichalcogenides MX_2. Blue and yellow spheres denote the metal (M) and chalcogenide (X) atoms, respectively. The highlighted hexagon indicates unit cell. (b) Sketch of the atomic structure of the monolayer TMDCs. Six vectors $\vec{A}_i^\pm$ connect nearest-neighbor M and X atoms with $i = 1, 2, 3$, separated by a distance $l = a/\sqrt{3}\cos\theta$ nm, a is lattice constant and θ is the angle between M-X bond and the M plane. (c) The first Brillouin zone and high-symmetry points Γ, K, and M of TMDCs in reciprocal space of the triangular lattice. Its primitive lattice vectors are $\vec{b}_1$ and $\vec{b}_2$.
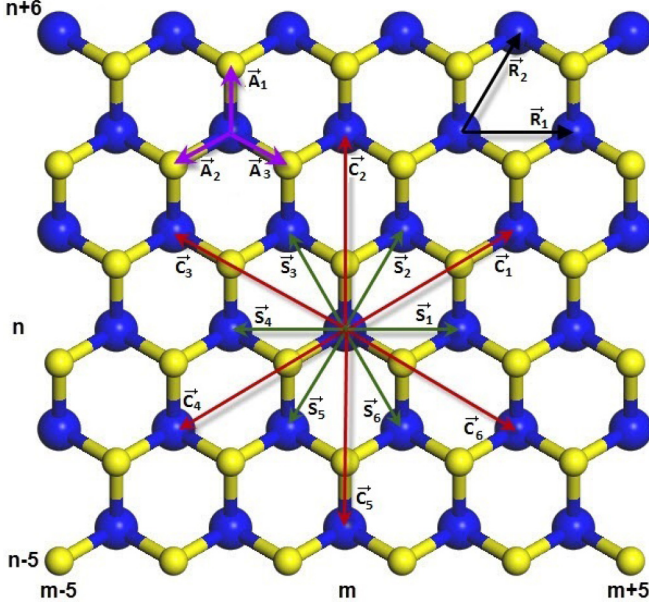
FIG. 2. Site-position coordinates of the monolayer transition-metal dichalcogenides MX_2. Blue and yellow spheres denote the metal (M) and chalcogenide (X) atoms, respectively. The green and red arrows represent the nearest-neighbor ($\vec{S}_i$) and next-nearest-neighbor ($\vec{C}_i$) M-M hopping vectors, respectively, where $i = 1, \ldots, 6$. The purple arrows indicate the nearest-neighbor M-X hopping vectors ($\vec{A}_j$) with $j = 1, \ldots, 3$. For illustration purpose, we only draw hopping vectors $\vec{A}_j$. Note that actually each of them are composed of two vectors $\vec{A}_j^{\pm}$, with $+$ ($-$) corresponding to the X atoms in the upper (lower) plane. $\vec{R}_1$ and $\vec{R}_2$ are basis vectors.

the contribution to the low-energy bands mainly comes from the d_{z^2}, d_{xy}, and $d_{x^2-y^2}$ orbitals. Then, the interactions between these d orbitals play an important role in low-energy subbands. Hence, in contrast to the SK TB models in literature, we added next-nearest-neighbor (NNN) interactions between M atoms in our theory. Aside from six nearest-neighbor (NN) S atoms (three on the top layer and the others on the bottom layer) as indicated by $\vec{A}_i$ vectors, $i = 1, 2, 3$, each Mo atom also interacts with six NN Mo atoms, see $\vec{S}_j$, and six NNN Mo-atoms, see $\vec{C}_j$ with $j = 1, \ldots, 6$ in Fig. 2. Notice that in this view two S atoms sit on top of each other. Table II summarizes the coordinates of hopping vectors considered in our model.

B. Eleven-band TB model for spin-degenerate TMDCs

We focus on periodic crystals and denote the lattice vectors by $\vec{R} = \vec{R}_I + \vec{R}_\tau$ where I and τ label the unit cells and the atoms ($\tau = $ Mo, S^t, and S^b with t and b indicating the top and bottom layers) within the unit cell. Bloch functions characterized by the crystal momentum $\vec{k}$ are expanded in the following way:

$$|\tau, \alpha_\tau, \vec{k}\rangle = \frac{1}{\sqrt{N}} \sum_{\vec{R}_I} e^{i\vec{k}\cdot(\vec{R}_I + \vec{R}_\tau)} \phi_{\alpha_\tau}(\vec{r} - \vec{R}_I - \vec{R}_\tau), \quad (1)$$

where N is the number of unit cells, and ϕ_{α_τ} denotes the α_τ orbital of τ atom, including five d orbitals of the M atom and

TABLE II. Hopping vectors used in our model and their respective coordinates relative to the site (m, n). $\vec{A}_i$ represent the nearest-neighbor M-X hopping vectors with $i = 1, \ldots, 3$, $\vec{S}_i$ and $\vec{C}_i$ correspond to the nearest-neighbor and next-nearest-neighbor M-M/X-X hopping vectors, respectively, as shown in Fig. 2, where $i = 1, \ldots, 6$, $l = a/(\sqrt{3} \cos\theta)$, $d = a\sqrt{3}$, and $\theta = 0.710$ rad *and a is lattice constant.*

Vector	Hopping	Coordinates
$\vec{A}_1^{\pm}$	$(m, n) \rightarrow (m, n+1)$	$l(0, \cos\theta, \pm\sin\theta)$
$\vec{A}_2^{\pm}$	$(m, n) \rightarrow (m-1, n-1)$	$l(-\frac{\sqrt{3}}{2}\cos\theta, -\frac{1}{2}\cos\theta, \pm\sin\theta)$
$\vec{A}_3^{\pm}$	$(m, n) \rightarrow (m+1, n-1)$	$l(\frac{\sqrt{3}}{2}\cos\theta, -\frac{1}{2}\cos\theta, \pm\sin\theta)$
$\vec{S}_1$	$(m, n) \rightarrow (m+2, n)$	$a(1, 0, 0)$
$\vec{S}_2$	$(m, n) \rightarrow (m+1, n+2)$	$a(\frac{1}{2}, \frac{\sqrt{3}}{2}, 0)$
$\vec{S}_3$	$(m, n) \rightarrow (m-1, n+2)$	$a(-\frac{1}{2}, \frac{\sqrt{3}}{2}, 0)$
$\vec{S}_4$	$(m, n) \rightarrow (m-2, n)$	$a(-1, 0, 0)$
$\vec{S}_5$	$(m, n) \rightarrow (m-1, n-2)$	$a(-\frac{1}{2}, -\frac{\sqrt{3}}{2}, 0)$
$\vec{S}_6$	$(m, n) \rightarrow (m+1, n-2)$	$a(\frac{1}{2}, -\frac{\sqrt{3}}{2}, 0)$
$\vec{C}_1$	$(m, n) \rightarrow (m+3, n+2)$	$d(\frac{\sqrt{3}}{2}, \frac{1}{2}, 0)$
$\vec{C}_2$	$(m, n) \rightarrow (m, n+4)$	$d(0, 1, 0)$
$\vec{C}_3$	$(m, n) \rightarrow (m-3, n+2)$	$d(-\frac{\sqrt{3}}{2}, \frac{1}{2}, 0)$
$\vec{C}_4$	$(m, n) \rightarrow (m-3, n-2)$	$d(-\frac{\sqrt{3}}{2}, -\frac{1}{2}, 0)$
$\vec{C}_5$	$(m, n) \rightarrow (m, n-4)$	$d(0, -1, 0)$
$\vec{C}_6$	$(m, n) \rightarrow (m+3, n-2)$	$d(\frac{\sqrt{3}}{2}, -\frac{1}{2}, 0)$

six p orbitals of the two X atoms in the unit cell, i.e., (p_x^t, p_y^t, p_z^t, $d_{3z^2-r^2}$, $d_{x^2-y^2}$, d_{xy}, d_{yz}, d_{zx}, p_x^b, p_y^b, p_z^b). In this basis set, the matrix form of the Hamiltonian reads as

$$\langle \tau', \alpha_{\tau'}', \vec{k}|H|\tau, \alpha_\tau, \vec{k}\rangle$$
$$= \sum_{\vec{R}_I} e^{i\vec{k}\cdot(\vec{R}_I + \vec{R}_\tau - \vec{R}_{\tau'})} t_{\alpha_{\tau'}, \alpha_\tau}(\vec{R}_I + \vec{R}_\tau - \vec{R}_{\tau'}) + \varepsilon_{\alpha_{\tau'}, \alpha_\tau} \delta_{\alpha_{\tau'}, \alpha_\tau}.$$
$$(2)$$

The dimension of the Hamiltonian matrix equals the total number of orbitals of M and X atoms within the unit cell, i.e., 11. $\varepsilon_{\alpha_{\tau'}, \alpha_\tau}$ denotes atomic energy of the τ atom, and $t_{\alpha_{\tau'}, \alpha_\tau}(\vec{R}_I + \vec{R}_\tau - \vec{R}_{\tau'})$ are the corresponding hopping integrals between the different orbitals, which are described in terms of σ, π, and δ ligands, respectively. The Bloch eigenfunctions $|n, \vec{k}\rangle$ are characterized by the index of the energy bands n and Bloch wave number $\vec{k}$. They are expanded in terms of the Bloch basis functions of Eq. (1) with coefficients $C_m(n, \mathbf{k})$ as follows:

$$|n, \vec{k}\rangle = \sum_{\tau, \alpha_\tau} C_m(n, \vec{k})|\tau, \alpha_\tau, \vec{k}\rangle, \quad (3)$$

where m is a compact index of (τ, α_τ). The TMDC crystal lattice possesses mirror inversion symmetry around the central layer under a $z \rightarrow -z$. It allows us to perform a unitary transformation, making the p orbitals of the top and bottom layers of the X atoms be their symmetric and antisymmetric combinations with respect to the z axis. The transformed atomic orbital bases which are used in our TB model and their symmetries under xy mirror reflection are listed in Table III.

TABLE III. Atomic orbitals used in TB model and their symmetry under xy mirror reflection ($M1$). t and b refer to the top- and bottom-layer X atoms. The index number refers to the order of the basis functions when we construct the Hamiltonian matrix. Even (odd) indicates the parity of the basis functions.

Index	Basis function	$M1$
1	d_{z^2}	
2	d_{xy}	
3	$d_{x^2-y^2}$	Even
4	$p_z^e = \frac{1}{\sqrt{2}}(p_z^t - p_z^b)$	
5	$p_x^e = \frac{1}{\sqrt{2}}(p_x^t + p_x^b)$	
6	$p_y^e = \frac{1}{\sqrt{2}}(p_y^t + p_y^b)$	
7	d_{xz}	
8	d_{yz}	
9	$p_z^o = \frac{1}{\sqrt{2}}(p_z^t + p_z^b)$	Odd
10	$p_x^o = \frac{1}{\sqrt{2}}(p_x^t - p_x^b)$	
11	$p_y^o = \frac{1}{\sqrt{2}}(p_y^t - p_y^b)$	

In this way, the 11-band model is decoupled into a 6×6 block with symmetry (antisymmetry) of the p_x and p_y (p_z) orbitals with respect to $z \to -z$ inversion, and a 5×5 block with an opposite combination. With this arrangement we can fit the bands related to the even and odd basis sets, separately. Therefore, although the Hilbert space is reduced, both the relevant conduction and valence bands around Fermi level are still well accounted for. Then, the matrix elements of the Hamiltonian for spinless fermions in TMDCs are given by

$$H_{\text{TB}} = \begin{pmatrix} H_E & 0 \\ 0 & H_O \end{pmatrix}, \qquad (4)$$

where $H_{E/O}$ referring to the matrix associated with the even/odd basis set is given by

$$H_{E/O} = \begin{pmatrix} M^{E/O} + H_{M-M}^{E/O} & H_{M-X}^{E/O} \\ H_{M-X}^{E/O\,\dagger} & X^{E/O} + H_{X-X}^{E/O} \end{pmatrix}, \qquad (5)$$

in which $M^{E/O}$ and $X^{E/O}$ stand for the onsite energy matrices, $H_{M-M}^{E/O}$ and $H_{X-X}^{E/O}$ represent the hopping matrices between the same type of atoms, and $H_{M-X}^{E/O}$ denotes the hopping matrices between different types of atoms. The corresponding expressions are shown in Appendix A.

C. Spin-orbit coupling

With the knowledge of the spin-degenerate TMDC band structure, we are ready to extend our study to the effect of spin-orbit interaction, which is usually missing in the TB calculation in literature. It can be done by adding the SOC term in the Hamiltonian of the system. We assume that the relativistic effects only affect intra-atomic Hamiltonian matrix elements, i.e., the SOC is assumed to couple only intra-atomic states with nonzero angular momentum. As demonstrated in the previous section, in an appropriate symmetrized form, the matrix of Hamiltonians can be divided into even H_E and odd H_O subblocks. The TMDCs with SOC can be described by

TABLE IV. Atomic orbitals used in the TB model with SOC and their symmetry under xy mirror reflection ($M1$). t and b refer to the top- and bottom-layer X atoms. The index number refers to the order of the basis functions when we construct the Hamiltonian matrix. Even (odd) indicates the parity of the basis functions.

Index	Basis function	Spin	$M1$
1	d_{z^2}	↑	
2	d_{xy}	↑	
3	$d_{x^2-y^2}$	↑	Even, ↑
4	$p_z^e = \frac{1}{\sqrt{2}}(p_z^t - p_z^b)$	↑	
5	$p_x^e = \frac{1}{\sqrt{2}}(p_x^t + p_x^b)$	↑	
6	$p_y^e = \frac{1}{\sqrt{2}}(p_y^t + p_y^b)$	↑	
7	d_{xz}	↑	
8	d_{yz}	↑	
9	$p_z^o = \frac{1}{\sqrt{2}}(p_z^t + p_z^b)$	↑	Odd, ↑
10	$p_x^o = \frac{1}{\sqrt{2}}(p_x^t - p_x^b)$	↑	
11	$p_y^o = \frac{1}{\sqrt{2}}(p_y^t - p_y^b)$	↑	
12	d_{z^2}	↓	
13	d_{xy}	↓	
14	$d_{x^2-y^2}$	↓	Even, ↓
15	$p_z^e = \frac{1}{\sqrt{2}}(p_z^t - p_z^b)$	↓	
16	$p_x^e = \frac{1}{\sqrt{2}}(p_x^t + p_x^b)$	↓	
17	$p_y^e = \frac{1}{\sqrt{2}}(p_y^t + p_y^b)$	↓	
18	d_{xz}	↓	
19	d_{yz}	↓	
20	$p_z^o = \frac{1}{\sqrt{2}}(p_z^t + p_z^b)$	↓	Odd, ↓
21	$p_x^o = \frac{1}{\sqrt{2}}(p_x^t - p_x^b)$	↓	
22	$p_y^o = \frac{1}{\sqrt{2}}(p_y^t - p_y^b)$	↓	

adding the following term in the H_{TB}:

$$H_{\text{SOC}} = \sum_\alpha \frac{\lambda_\alpha}{\hbar} \vec{L}_\alpha \cdot \vec{S}_\alpha, \qquad (6)$$

where λ_α is the intrinsic SOC strength for an α atom ($\alpha = M$ or X type), $\vec{L}_\alpha$ is the atomic orbital angular momentum operator, and $\vec{S}_\alpha$ is the electronic spin operator. Taking into account the spin degree of freedom, the number of basis functions is doubled, as shown in Table IV.

Explicitly, the matrix form of the Hamiltonian for the monolayer TMDCs is given by

$$H = \begin{pmatrix} H_{\text{TB}} & 0 \\ 0 & H_{\text{TB}} \end{pmatrix} + \begin{pmatrix} H_{\text{SO}}^{\uparrow\uparrow} & H_{\text{SO}}^{\uparrow\downarrow} \\ H_{\text{SO}}^{\downarrow\uparrow} & H_{\text{SO}}^{\downarrow\downarrow} \end{pmatrix}, \qquad (7)$$

where

$$H_{\text{SO}}^{\uparrow\uparrow} = \begin{pmatrix} H_{\text{SO1}}^{\uparrow\uparrow} & 0 \\ 0 & H_{\text{SO2}}^{\uparrow\uparrow} \end{pmatrix}, \quad H_{\text{SO}}^{\uparrow\downarrow} = \begin{pmatrix} 0 & H_{\text{SO1}}^{\uparrow\downarrow} \\ H_{\text{SO2}}^{\uparrow\downarrow} & 0 \end{pmatrix},$$

$$H_{\text{SO}}^{\downarrow\uparrow} = \begin{pmatrix} 0 & H_{\text{SO1}}^{\downarrow\uparrow} \\ H_{\text{SO2}}^{\downarrow\uparrow} & 0 \end{pmatrix}, \quad H_{\text{SO}}^{\downarrow\downarrow} = \begin{pmatrix} H_{\text{SO1}}^{\downarrow\downarrow} & 0 \\ 0 & H_{\text{SO2}}^{\downarrow\downarrow} \end{pmatrix}. \qquad (8)$$

The complete definition of the SOC matrices is shown in Appendix B, and a separated set of SOC parameters are listed in Table V. Since low-energy excitations belong exclusively to the first block, the fit to DFT that we will present later will

TABLE V. Atomic SOC parameters in eV for transition metals (α = Mo, W) and chalcogenides (α = S, Se, Te).

α	Mo	W	S	Se	Te
λ_α	0.0806	0.2754	0.0536	0.0820	0.1020

be performed within this section. We are solving a generalized eigenvalue problem, where the description of the Hamiltonian and overlap matrix for the TMDCs is attained by employing a set of TB fitting parameters that describe the onsite orbital energies, the two-center SK energy integrals, overlap integrals, and SOC, which is assumed to couple only intra-atomic states with nonzero angular momentum.

In analog to the spin-degenerate (zero SOC) case, first, we perform DFT simulation, using QUANTUM ESPRESSO [18], with GGA exchange-correlation functional, full-relativistic PBE pseudopotentials, and Monkhorst-Pack $15 \times 15 \times 2$. Then, we implement our 22-band TB model. After that, we perform the best fitting of our TB results to the DFT calculated band splitting in the valence band around the K point. Finally, we do overall band structure fitting to determine TB parameters.

D. Description of DFT calculation

To get a reference for making comparison, we have used the DFT as implemented in QUANTUM ESPRESSO package [18]. In this framework, the electronic wave functions are expanded in a plane-wave basis set with the energy cutoff of 1360 eV. The core of atoms is replaced by pseudopotentials with/without fully relativistic effects with an additional information for spin-orbit calculations. The reference of valence ground states for pseudopotential generation for S, Mo, Se, Te, and W are $(3s^2, 3p^4)$, $(4s^2, 4p^6, 4d^5, 5s^1)$, $(4s^2, 4p^4)$, $(4d^1, 5s^2, 5p^4)$, and $(5s^2, 5p^6, 5d^4, 6s^2)$, respectively. The exchange-correlation effects are included through the generalized gradient approximation (GGA) proposed by Perdew *et al.* (PBE) [37]. For the Brillouin-zone sampling, we used a grid of $15 \times 15 \times 2$ k points. The convergence criteria used for self-consistent calculation was 10^{-8} atomic units.

E. TMDC zigzag NRs

When the geometry of the TMDCs is changed, interesting phenomena and novel properties may arise [38]. For instance, when the monolayer MoS_2 is patterned into NR, it changes from a semiconductor to metallic one. In addition, it also exhibits ferromagnetic behavior [39,40]. In contrast, as the MoS_2 is going from monolayer bulk material to an armchair NR, mid-gap edge states emerge, but they present nonmagnetic and semiconducting characteristics. When the ribbon width increases, the band gaps converge to a constant value of 0.56 eV. Although the physical properties of the MoS_2 NRs are widely studied both experimentally and theoretically, the knowledge about other TMDC NRs is still in the early infancy. As known, the most straightforward method to study finite-size effects is a lattice model in real space. The *ab initio* simulations and TB method are two powerful lattice-based models. In comparison with the latter, the former method takes much more computational time, especially for wider NRs. Here, as an
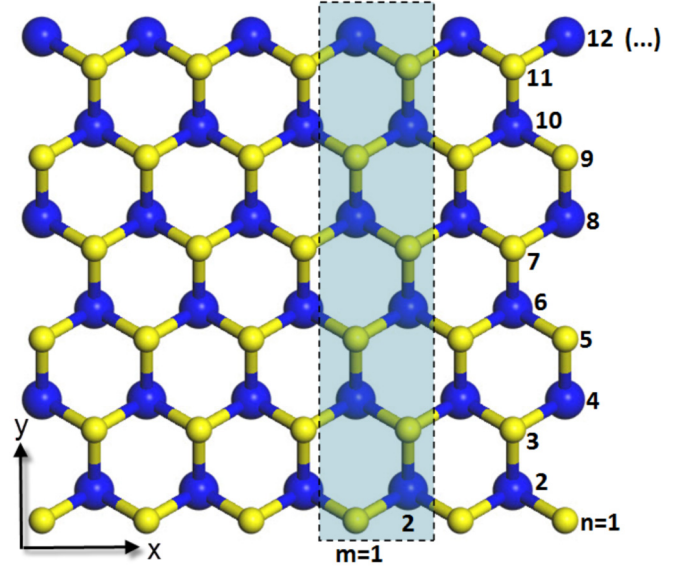

FIG. 3. Top view of lattice structure of monolayer MX_2 in which the zigzag and armchair directions are illustrated. The shaded area indicates the unit cell of a zigzag NR. The positions of lattice sites are defined by coordinates (m, n).

application, let us extend our TB model for monolayer TMDC to the NRs to predict the overall band structures for five NRs of the most studied monolayer TMDCs.

As we did in the case of monolayer bulk TMDCs, here we also use the lattice coordinates shown in Fig. 2 to determine the site positions of zigzag NRs. Nevertheless, now our unit cell becomes much larger than that of former case because of breaking translational symmetry along the $\hat{x}$ direction. It is illustrated by the shaded rectangular area in Fig. 3 which is defined by m and n indices, where $m = 1, 2$, and $n = 1, 2,...,n_{max}$. The n_{max} corresponds to the number of the sites in the unit cell. The low- (high-) energy band structure of the system belongs to the even (odd) subspace [22]. In order to reduce the computational cost, but do not lose essential physics, only the even part of the Hamiltonian in the TB calculation of zigzag NRs is required to get the band structure near the Fermi level. In addition, since diagonal terms $\sim L_z S_z$ are dominant as compared to the off-diagonal spin-flip terms due to the fact that such spin-flip processes involve virtual transitions towards high-order energy states [22,41], spin-up and -down states in this case are decoupled. This allows us to reduce further the Hilbert space by dividing the spin-up and -down subspaces to solve them separately. The Hamiltonian reads as

$$H^{ZZ}(\tau) = \begin{pmatrix} M^{ZZ}(\tau) + H^{ZZ}_{M\text{-}M} & H^{ZZ}_{M\text{-}X} \\ H^{ZZ}_{X\text{-}M} & X^{ZZ}(\tau) + H^{ZZ}_{X\text{-}X} \end{pmatrix}. \quad (9)$$

The complete definition of the Hamiltonian matrices for zigzag NRs is shown in Appendix C.

F. TMDC armchair NRs

After studying zigzag NRs, let us turn our attention to the armchair ones. We assume that the transport direction is in $\hat{y}$ direction and a confinement is applied along the x axis with a width defined by m_{max}. The band gap and energy levels depend
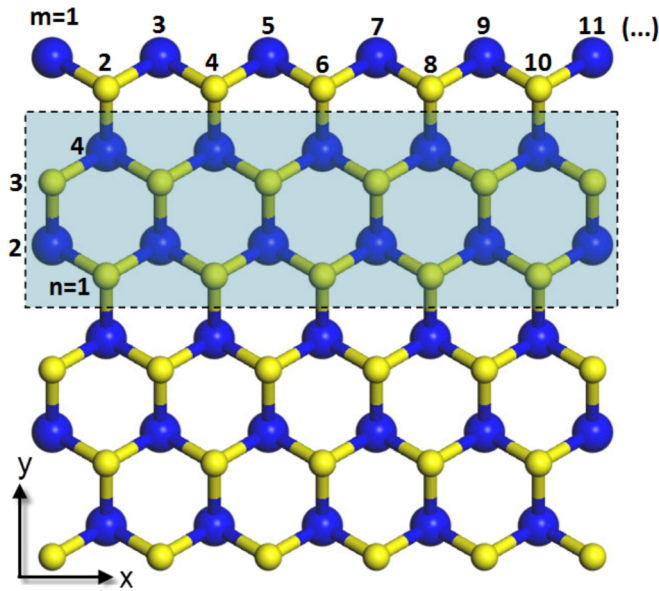
FIG. 4. Top view of lattice structure of monolayer MX_2 in which the zigzag and armchair directions are illustrated. The shaded area indicates the unit cell of an armchair NR. The positions of lattice sites are defined by coordinates (m, n).

on the width. As an example, we choose $m_{max} = 200$ to present our TB outcome. In ananalog to the case of zigzag NRs, here we also use the lattice coordinates shown in Fig. 2 to determine the site positions. The unit cell is illustrated by shaded rectangular area in Fig. 4 which is defined by m and n indices, where $m = 1, 2,...,m_{max}$ and $n = 1, 2,...,4$. Then, the number of the sites in the unit cell is equal to $2m_{max}$. In order to reduce the computational cost, only the even part of the Hamiltonian in the TB model is used to perform the calculation, as has been done in zigzag NRs. Interestingly, in this approximation, the spin-up and -down states become degenerated. Then, the Hamiltonian reads as

$$H_{AC}(\tau) = \begin{pmatrix} M^{AC}(\tau) + H_{M-M}^{ZZ} & H_{M-X}^{AC} \\ H_{X-M}^{AC} & X^{AC}(\tau) + H_{X-X}^{AC} \end{pmatrix}. \quad (10)$$

The complete definition of the Hamiltonian matrices for armchair NRs is shown in Appendix D.

III. RESULTS AND DISCUSSION

A. Band structure of MoS₂ obtained by different TB models

In order to develop an improved TB model, we analyze the advantage and disadvantage of seven widely accepted TB models in literature by a comprehensive comparison between the results of the TB and that of the DFT. They are the 3-band nearest-neighbor (NN) TB model with 8 hopping parameters and the 3-band TB model with up to third-nearest-neighbor (TNN) hoppings and 19 parameters by Xiao *et al.* [21], 5-band model with 28 parameters by Wu *et al.* [1], 6-band model with 11 parameters by Rostami *et al.* [22,27], 11-band TB model with 12 parameters by Capeluti *et al.* [23], 11-band TB model with 12 parameters by Ridolfi *et al.* [25], and 11-band TB model with 36 parameters by Fang *et al.* [24]. To do so, first, we have performed the first-principles calculation for the band

structure of the monolayer MoS₂ (see Sec. II D). Then, we do the same calculation, but by means of the aforementioned TB models. The corresponding outcomes are shown in Fig. 5. The red dots and blue curves represent the results of the former and the latter, respectively. After that, we make a comprehensive comparison between them.

Figures 5(a) and 5(b) plot the band structure of the monolayer MoS₂, produced by the three-band model in which only the d-atomic orbitals with the index number from 1 to 3 in Table III are employed [21]. In Fig. 5(a), only the NN M-M hoppings are accounted, while in Fig. 5(b) up to TNN M-M hoppings are taken into consideration. Group theory is used to define the hopping parameters. Notice that the NN model gives rise to a well-fitted highest valence band (VB) (see the blue curve and its related red dots). However, except for the states nearby the K point, it does not produce an expected band structure for the other energy bands, even for the lowest conduction band (CB) [see Fig. 5(a)]. In contrast, the TNN model with 19 parameters [see Fig. 5(b)] achieves much better overall fit to the DFT results for all three energy bands, including two CBs and one VB [21]. It hints that the NN and TNN M-M hoppings play an important role [3,5,6,42]. On the other hand, since only d orbitals of M atoms were employed in a construction of these two models, they are not applicable to the systems with defects introduced by X atoms in the lattice, and are difficult to be extended to the confined finite systems with low geometric symmetry.

Figure 5(c) depicts the band structure of the monolayer MoS₂ obtained by five-band model of Wu *et al.* [1]. The Bloch wave functions of an electron are constructed by five d-atomic orbitals with the index number from 1 to 3, 7, and 8 in Table III. In this model, both the NN and TNN M-M hoppings are taken into account, involving 28 parameters which are also defined by the group theory. Notice that the five electronic bands including four CBs and one VB, produced by this TB calculation, are all well fitted to the DFT red dots. The improvement of the five-band TB calculation in comparison with the three-band model indicates that an increase in the number of d orbitals is benefit to the precision of outcome. However, the flexibility of the model is also limited due to asymmetry of d orbitals, as previous cases [28].

Figure 5(d) displays the results obtained by Rostami *et al.* [22] using six basis functions with index number from 1 to 6 in Table III and the SK two-center approximation to define 11 hopping parameters. Although not all of six energy bands are well fitted, both the lowest CB and highest VB present good curve fitting, especially in the vicinity of the K point. Hence, it gives rise to reliable effective masses of both electron and hole at the K point. Since the model is constructed directly in real space of the TMDCs and few parameters generated, it can be easily implemented and straightforwardly extended to other structures such as the NRs [39].

Figure 5(e) shows the band structure of the monolayer MoS₂ produced by an 11-band model of Capellutti *et al.* [23]. Eleven basis functions wth index number from 1 to 11 in Table III and the SK two-center approximation are utilized. The main advantages of this model are small number of the TB parameters (only 12) and easiness to be generalized to the multilayer, the bulk, and other geometries. On the other hand, since only the nearest-neighbor M-X, M-M, and X-X
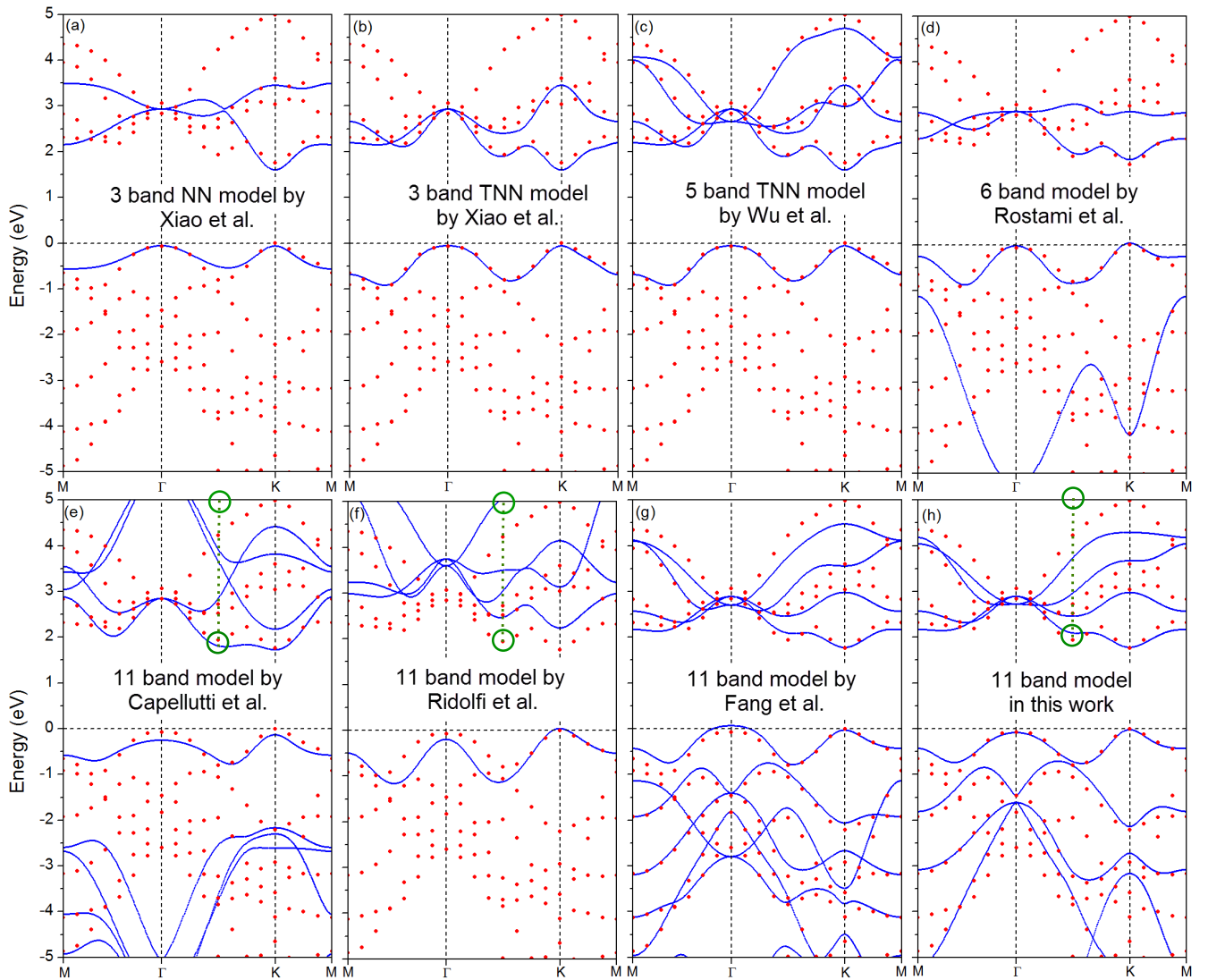
FIG. 5. Spin-degenerate band structures of monolayer MoS$_2$ along the path M-Γ-K-M, obtained by DFT calculation (red dots) with GGA-PBE pseudopotential and Monkhorst-Pack $15 \times 15 \times 2$ from QUANTUM ESPRESSO [18] and by TB models (blue curves). (a) Three-band nearest-neighbor model with 8 parameters by Xiao *et al.* [21], (b) 3-band third-nearest-neighbor model with 19 parameters by Xiao *et al.* [21], (c) 5-band model with 28 parameters by Wu *et al.* [1], (d) 6-band model with 11 parameters by Rostami *et al.* [22,27], (e) 11-band model with 12 parameters by Capellutti *et al.* [23], (f) 11-band model with 12 parameters by Ridolfi *et al.* [25], (g) 11-band model with 36 parameters by Fang *et al.* [24], and (h) 11-band model with 31 parameters in this work. In (e), (f), and (h), where the 11-band TB calculations are all based on the SK method, the dotted green line bridging two green circles represents the location of Q point in momentum space.

hoppings are taken into account, as the model by Rostami *et al.* [22], it hardly predicts an accurate band structure, except for the lowest CB and the highest VB. For instance, in most of k points, the curves of both higher-energy bands in the CB and lower ones in the VB are far away from corresponding DFT data (red dots).

Let us turn our attention to the band structure which is shown in Fig. 5(f) calculated by the model of Ridolfi *et al.* [25]. This model is similar with the one developed by Capellutti *et al.* [23]. While its TB parameters are determined by fitting to DFT data obtained by utilizing the HSE06 exchange-correlation functional, instead of GGA-PBE.

Figure 5(g) plots outcome of the model proposed by Fang *et al.* Eleven atomic orbitals with the index number from 1 to 11 in Table III are employed [24]. In this model, both the nearest-

and next-nearest M-X hoppings are taken into account, while only nearest M-M and X-X hoppings are considered. The group theory is used to define 36 TB parameters. Notice that except for some points along the M-Γ-K-M path such as around the Γ point, it predicts a well-fitted band structure for all 11 electronic bands. Hence, generally speaking, it is a TB model with the highest accuracy to date. However, as the other TB models based on the group theory, it is also difficult to be extended to the confined finite systems with low symmetry, such as NRs and quantum dots [28].

In Fig. 5(h), we show the band structure calculated by our proposed 11-band model in which we utilize all the basis functions listed in Table III and the 31 SK parameters given in Tables VI and VII. Since the existing SK models in literature only include the NN M-M and X-X hoppings, they can only

TABLE VI. SK even parameters in eV used in our TB calculation for monolayer MX_2. The index e/o indicates the even/odd part of Hamiltonian, the E_{d0}^e and E_{d1}^e are onsite energies of d_{z^2} and d_{xy} ($d_{x^2-y^2}$) orbitals of M atom, respectively. E_{s1}^e and E_{s2}^e are onsite energies of the p_x^e (p_Y^e) and p_Z^e orbitals of X atom. The V hopping parameters represent the nearest-neighbor parameters for the interactions of M-M, X-X, and M-X atoms, the K's represent the second-nearest neighbor M-M and X-X hopping parameters.

	MoS$_2$	MoSe$_2$	MoTe$_2$	WS$_2$	WSe$_2$
E_{d0}^e	−0.4939	−0.1276	−0.6630	−0.3609	−0.5558
E_{d1}^e	−0.2473	−0.2724	−0.2852	−0.7364	−1.934
E_{s1}^e	−4.5716	−6.1588	−0.5923	−5.0982	−2.9498
E_{s2}^e	−8.3498	−7.3399	−3.7035	−9.4019	−6.5922
$V_{pd\pi}^e$	−1.2413	−1.4295	−0.6279	−1.2119	−0.9139
$V_{pd\sigma}^e$	4.2398	3.4524	2.2362	5.2769	5.1750
$V_{pp\sigma}^e$	−0.0914	1.2630	0.8198	−0.3943	0.1311
$V_{pp\pi}^e$	−0.4619	−0.4857	−0.2483	−0.4069	−0.2475
$V_{dd\sigma}^e$	−0.6717	−0.6674	−0.4795	−0.8942	−0.8697
$V_{dd\pi}^e$	0.5706	0.5573	−0.0934	0.7347	0.6206
$V_{dd\delta}^e$	0.2729	0.0970	0.1656	0.3417	0.3743
$K_{pp\sigma}^e$	0.3723	0.2372	0.1169	0.1415	0.1197
$K_{pp\pi}^e$	0.0014	0.0249	0.2683	0.0261	0.1075
$K_{dd\sigma}^e$	0.0314	0.0776	−0.1493	0.0508	0.0443
$K_{dd\pi}^e$	0.0961	0.0573	−0.0627	0.1278	0.0912
$K_{dd\delta}^e$	−0.0305	−0.04778	0.0360	−0.0091	−0.0447

produce reliable band structure for few energy bands. In this work, we go one step further, the orbital symmetry and up to next-NN hoppings between the M-M and X-X atoms are taken into consideration. It is worth recalling that in the fitting procedure, we notice that as other two-dimensional van der Waals materials, the stronger interactions take place between

TABLE VII. SK odd parameters in eV used in our TB calculation for monolayer MX_2. The index e/o indicates the even/odd part of Hamiltonian, E_{d2}^o is onsite energy of d_{xz} or d_{yz} orbital of M atom, E_{s1}^o and E_{s2}^o are onsite energies of the p_x^o (p_y^o) and p_z^o orbitals of X atom, respectively. The V's represent the nearest-neighbor parameters for the interactions of M-M, X-X, and M-X atoms, the K's represent the second-nearest-neighbor M-M and X-X hopping parameters.

	MoS$_2$	MoSe$_2$	MoTe$_2$	WS$_2$	WSe$_2$
E_{d2}^o	0.5624	0.3046	0.0491	0.8877	0.6233
E_{s1}^o	−1.5251	−1.3298	−1.3905	−1.8175	−1.5016
E_{s2}^o	−0.6737	−0.9459	−0.0094	−1.0191	−1.4824
$V_{pd\pi}^o$	−0.7614	−0.6811	−0.5048	−0.8115	−0.7688
$V_{pd\sigma}^o$	2.2251	2.0197	1.8294	2.4044	2.1733
$V_{pp\sigma}^o$	0.8131	0.9449	0.8459	0.8415	0.9703
$V_{pp\pi}^o$	−0.2763	−0.3039	−0.4143	−0.2661	−0.2920
$V_{dd\sigma}^o$	−0.8950	−0.8950	−0.8950	−0.8950	−0.8950
$V_{dd\pi}^o$	0.0150	0.01637	0.3267	−0.0142	−0.0469
$V_{dd\delta}^o$	0.0497	0.0965	0.3033	0.0036	0.0923
$K_{pp\sigma}^o$	−0.0395	−0.0293	0.0114	−0.0169	−0.0451
$K_{pp\pi}^o$	0.0092	−0.0094	−0.0092	0.0262	0.0113
$K_{dd\sigma}^o$	0.0100	0.0100	0.0100	0.0100	0.0100
$K_{dd\pi}^o$	0.0051	0.0140	−0.0617	−0.0135	0.0096
$K_{dd\delta}^o$	0.0184	0.0354	0.1002	−0.0191	0.0140

atoms in the same plane. Hence, the next-NN M-X hopping parameters are too small to be considered. The NN M-X hoppings are good enough for the precision of TB calculation. It is also worthy to remark that in order to get an accurate band structure for energy bands close to Fermi level, we have to sacrifice the precision of the others. In this way, we obtain eight well-fitted energy bands [see Fig. 5(h)]. It is not difficult to notice that in comparison with the band structure produced by the other SK TB models, a significant improvement has been achieved. Finally, it is also important to point out that unlike TB model based on group theory, our model possesses high flexibility. It is worth noting that our computed electronic band structure fits well to the DFT calculation not only around the K (K') point, but also around the Q point [cf. fittings along the dotted green line connecting two green circles in Figs. 5(e), 5(f), and 5(h)], where all TB calculations are based on the SK method, indicating the importance of the next-NN hopping between the M-M and X-X atoms.

Through this comprehensive analysis of different TB models, we can then conclude that the accuracy of the outcome of a TB model depends on the number of atomic basis functions, whether only to NN or up to next-NN M-M and X-X hoppings, and the way to build it. For the TB models using incomplete basis function (less than 11 bases), the density of states as well as other relevant physical quantities which depend on the wave functions could not be properly described. Besides, they are hardly generalized to study the disordered systems such as the TMDCs with vacancies. Hence, the complete basis functions are in high demand. On the other hand, because the stronger interactions take place between atoms in the same plane, both NN and next-NN M-M and X-X hoppings play an important role. The SK models can be straightforwardly extended to study the disordered TMDCs, the NR, and quantum dots. Usually, the TB models based on group theory can provide better fittings than that of corresponding SK models. However, it is difficult to be extended to the confined finite systems with lower symmetry.

B. Band structures of monolayer MX_2 obtained by DFT and our TB model

Figure 6 plots the electronic band structures of monolayer MX_2 from our nonrelativistic TB model in which no SOC exists. They are 2D subbands with direct band gaps at band edges located at the highly symmetric K and K' points in momentum space. In valence bands, the subbands around the Γ point are stemmed from the d_0 orbital while subbands around the K and K' valleys resulting from the d_{-2} and d_2 orbitals, respectively. In contrast, in conduction bands, only d_0 orbital appears around the K and K' valleys. Notice that for a given transition-metal species, as the atomic indices of chalcogen species increase from S to Te, the conduction band edge undergoes a conspicuous energy increase, accompanied by a relatively smaller energy increase of valence band edge, giving results to a reduction of energy gap. Since an increase in the atomic indices of chalcogen atoms leads to a larger atomic radius and decreased reactivity, the lattice constant is enlarged. Then, the interatomic interaction strength becomes weakened. Thus, a smaller band gap is expected. On the other hand, for a given chalcogen species, Mo is more reactive than W due to the
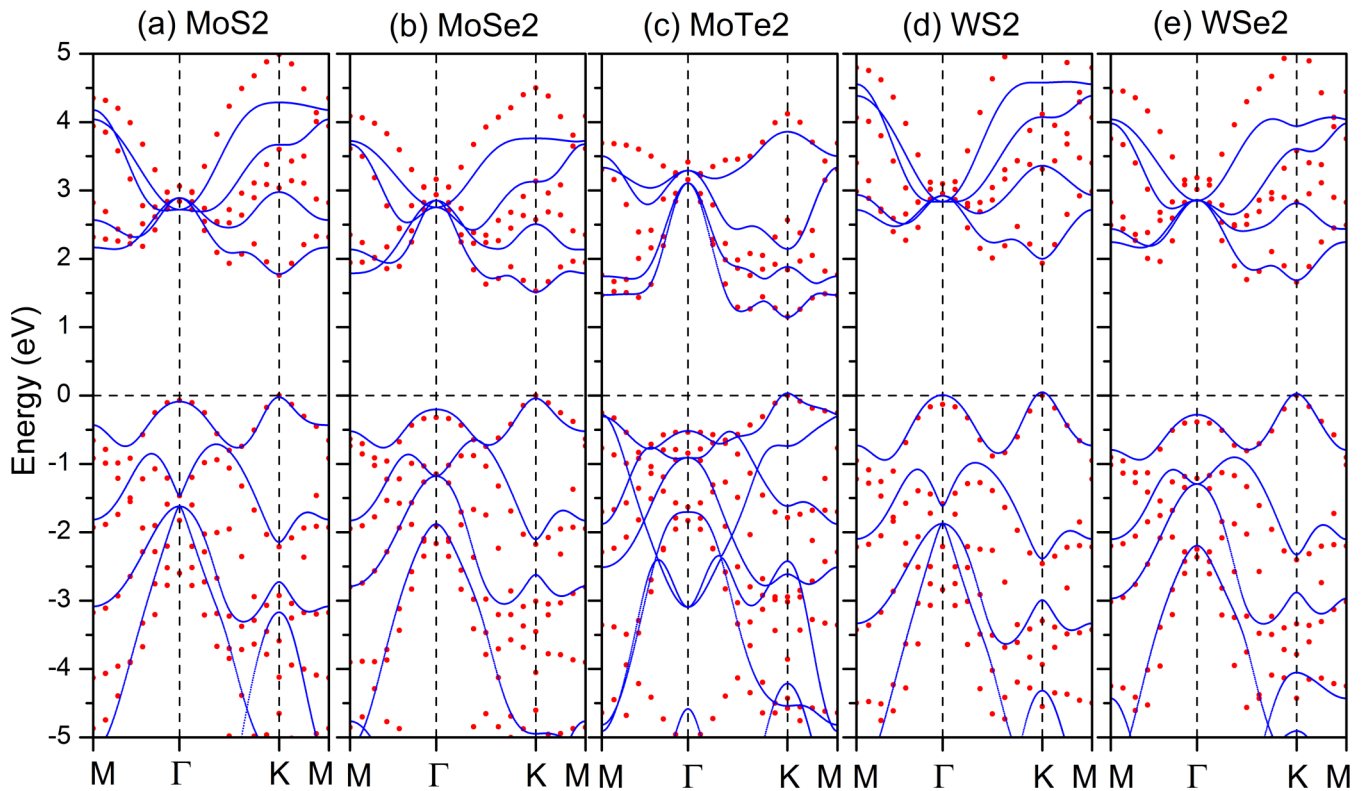
FIG. 6. Spin-degenerate band structures along the path M-Γ-K-M of monolayer MoS$_2$ (a), MoSe$_2$ (b), MoTe$_2$ (c), WS$_2$ (d), and WSe$_2$ (e), respectively, obtained by DFT calculation using QUANTUM ESPRESSO [18] with GGA-PBE pseudopotential and Monkhorst-Pack $15 \times 15 \times 2$ (red dots) and by our TB model (blue curves).

intrinsic higher reactivity of $3d$ electrons in comparison with $4d$ electrons. Hence, the overall energy levels of Mo-based TMDCs are lower than that of W-based ones.

The spin degeneracy can be effectively split by the intrinsic SOC, as shown in Fig. 7 in which we show band structures along the path M-Γ-K-M of monolayer MoS$_2$ (a), MoSe$_2$ (b), MoTe$_2$ (c), WS$_2$ (d), and WSe$_2$ (e), respectively, with spin-orbit coupling, obtained by DFT calculation using QUANTUM ESPRESSO [18] with GGA-PBE full-relativistic pseudopotential and Monkhorst-Pack $15 \times 15 \times 2$ (red dots), and by our TB model (blue curves). The splitting is quite evident for valence bands near the K and K' points. Nevertheless, it is small elsewhere. In the K valley, the SOC drives spin-up and -down states, respectively, shift up and move down by λ. Then, the splitting between these two opposite spin states is equal to 2λ. In the K' valley, however, the spin-up (down) state becomes a lower- (higher-) energy state (not shown in Fig. 7). Hence, the energy levels of spin-up and -down states are interchanged with moving from valley K to K' due to time-reversal symmetry, which enables the manipulation of the combined spin and valley degrees of freedom in such an atomic thin layer. It is interesting to recall that the ordering of the lowest spin-up and -down states in the conduction band near the K and K' points of the MoX_2 is opposite to that of WX_2 due to the SOC. Since optical transitions do conserve the spin, different orderings of electronic conduction bands have profound consequences on their optical properties. For instance, the spin configuration for the top valence band and the lowest conduction band of the M dichalcogenides is parallel, between which the optical

transition is allowed. Then, the excitonic ground state is bright. Nevertheless, for the W dichalcogenides, the corresponding spin configuration is antiparallel. Then, the interband transition is optically forbidden. Hence, the excitonic ground state is dark.

To gain a deep insight into the features of the band structures presented in Fig. 7, we have calculated density of states of the monolayer MX_2 whose outcome is depicted at right-hand side in Fig. 8. For convenience, the corresponding band structure is also exhibited (see the right-hand side of the figure). It is worthwhile to remark that the contributions of the most relevant orbitals ($d_{3z^2-r^2}$, $d_{x^2-y^2}$, d_{xy}, p_x, p_y, p_z) to the density of states, shown in Fig. 8, reproduce the DFT results at the most important points of the band structure. Therefore, our TB model presents not only reliable band structure, but also acceptable wave functions.

C. Topological features of TMDC NRs

Figure 9 shows the energy dispersions of MoS$_2$, MoSe$_2$, MoTe$_2$, WS$_2$, and WSe$_2$ zigzag NRs with the same width defined by $n_{max} = 200$ along the y direction. To gain a deep understanding of the band structure, let us focus our attention on the states located at crossing points of dashed vertical line with the energy band curves of the NR. For instance, the states labeled by A, B, C, C', and D in Fig. 9(b). We find that the A and D are bulk states in the CB and VB, respectively, because their orbital characters are consistent with that of the bulk spectrum. While the other three states marked by B, C, and C' are edge
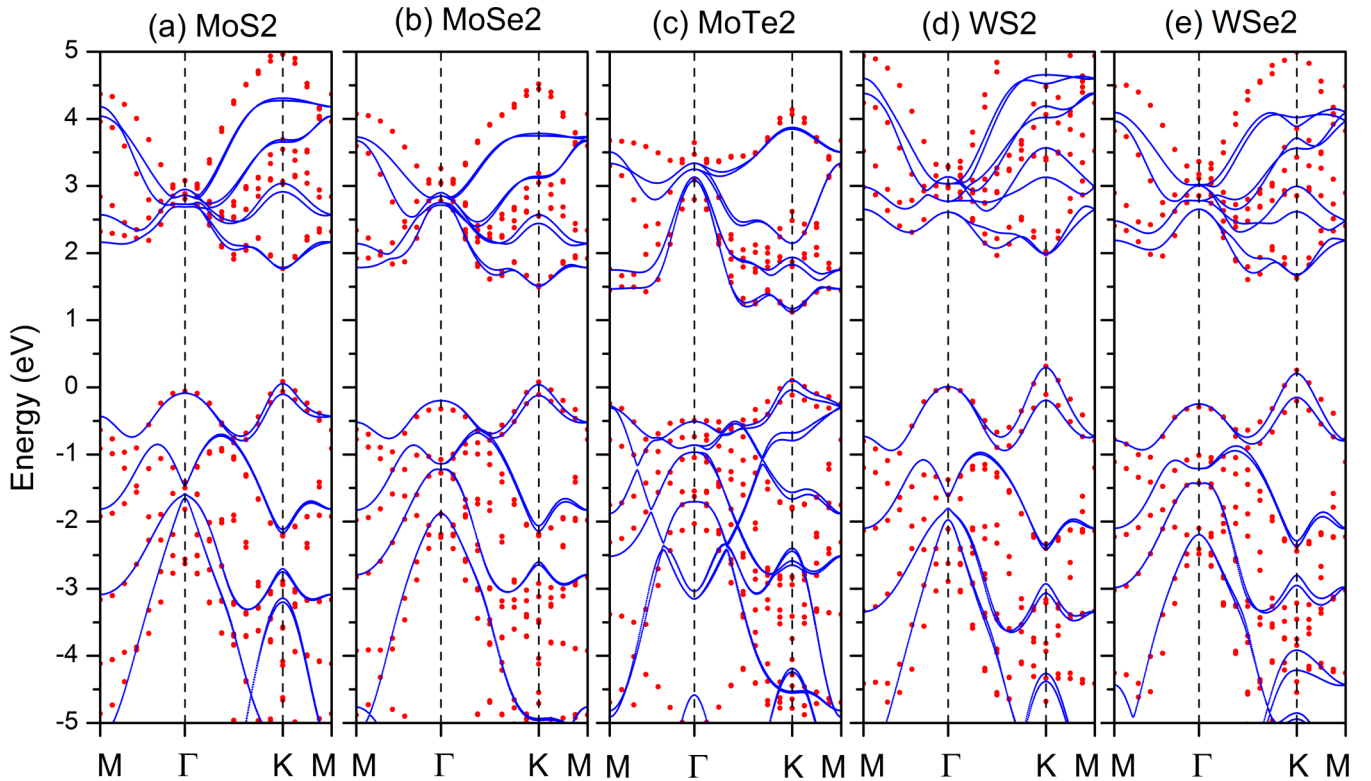
FIG. 7. Band structures along the path M-Γ-K-M of monolayer MoS$_2$ (a), MoSe$_2$ (b), MoTe$_2$ (c), WS$_2$ (d), and WSe$_2$ (e), respectively, with spin-orbit coupling, obtained by DFT calculation using QUANTUM ESPRESSO [18] with GGA-PBE full-relativistic pseudopotential and Monkhorst-Pack $15 \times 15 \times 2$ (red dots), and by our TB model (blue curves) for (a) MoS$_2$, (b) MoSe$_2$, (c) MoTe$_2$, (d) WS$_2$, and (e) WSe$_2$, respectively.

modes. Among them, the B state has mostly d-orbital character while the C and C$'$ states are mostly from p_x and p_y orbitals of sulfur atoms and d_{z^2} orbitals of molybdenum atoms. Besides, the C and C$'$ are located on one edge of the NR, but the B state is on the opposite edge. Interestingly, an analogical analysis is applicable to all the other TMDC NRs such as the one shown in Fig. 9(d). Hence, there are three spin-splitted edge modes plotted by blue (spin-up) and red (spin-down) dotted curves within the bulk gap. Note that one-dimensional (1D) Dirac cones are formed due to crossovers of different edge modes. While the number and locations of these 1D Dirac cones for the two spin and two valley flavors depend strongly on the chemical composition of the MX_2. In addition, also note that some zigzag TMDC NRs such as MoS$_2$, WS$_2$, and MoTe$_2$ are of metallic behavior. Nevertheless, others, e.g., MoSe$_2$ and WSe$_2$, their edge modes exhibit finite gaps. In other words, not all of the TMDC zigzag NRs present metallic behavior, instead, they might be semiconducting. This is in contradiction to the usual consensus concerning the zigzag TMDC NRs being metallic [22,43,44]. It is worthy to recall that although the result of the 11-band TB model by Fang *et al.* [24] does fit quite well band structures of the monolayer TMDCs produced by the DFT calculation, it could not predict zero-gap edge modes.

The upper panels in Fig. 10 display the zoom of the edge modes around Fermi level of the monolayer TMDC NRs indicated by a dashed horizontal line. A, B, C, and D are crossing points of the energy dispersion curves with the Fermi level. The probability distributions of these four edge states are calculated by our TB model whose results are schematically shown in the lower part of Fig. 10. We find that the number of the states at Fermi level and their location depend strongly on chemical composition of the NR. More specifically, there are four edge states at Fermi level in MoS$_2$ NR for each spin component. Among them, A and D states are located in the upper edge of the ribbon, while B and C states are in the opposite edge as shown in Fig. 10(f). In contrast, only two edge states A and D are found in either MoSe$_2$ or MoTe$_2$ NR. Both of them are located at the upper edge of the ribbon [see Fig. 10(g)]. For the WS$_2$ NR, there are also two edge states. Nevertheless, they are located at the lower edge of the ribbon. There are four edge states in the WSe$_2$ NR, similar to the MoS$_2$ NR. However, the movement of an electron in either B or C state in Fig. 10(i) is along an opposite direction with the corresponding one in Fig. 10(f). Aside from these differences, the most prominent distinctions among the five NRs are in the following. At the first glare, Fig. 10(f) seems similar to Fig. 10(i). Actually, they exhibit totally different physics. In the former case (the MoS$_2$ NR), the four edge states are distributed in two 1D valleys in such a way that A and B are in the valley V_1, and C and D states in the V_2, as illustrated in inset of Fig. 10(f). As will be discussed below, movement of electrons in these edge states leads to valley Hall effect. In the latter case, however, no valley Hall effect could be expected. Now, let us make an insight analysis for the edge states in the MoS$_2$ NR, shown in Fig. 10(f). It is intriguing to note that the edge modes in different valleys circulate in two opposite directions, leading to a weak topological insulator phase for each spin flavor. Notice also that in each 1D valley
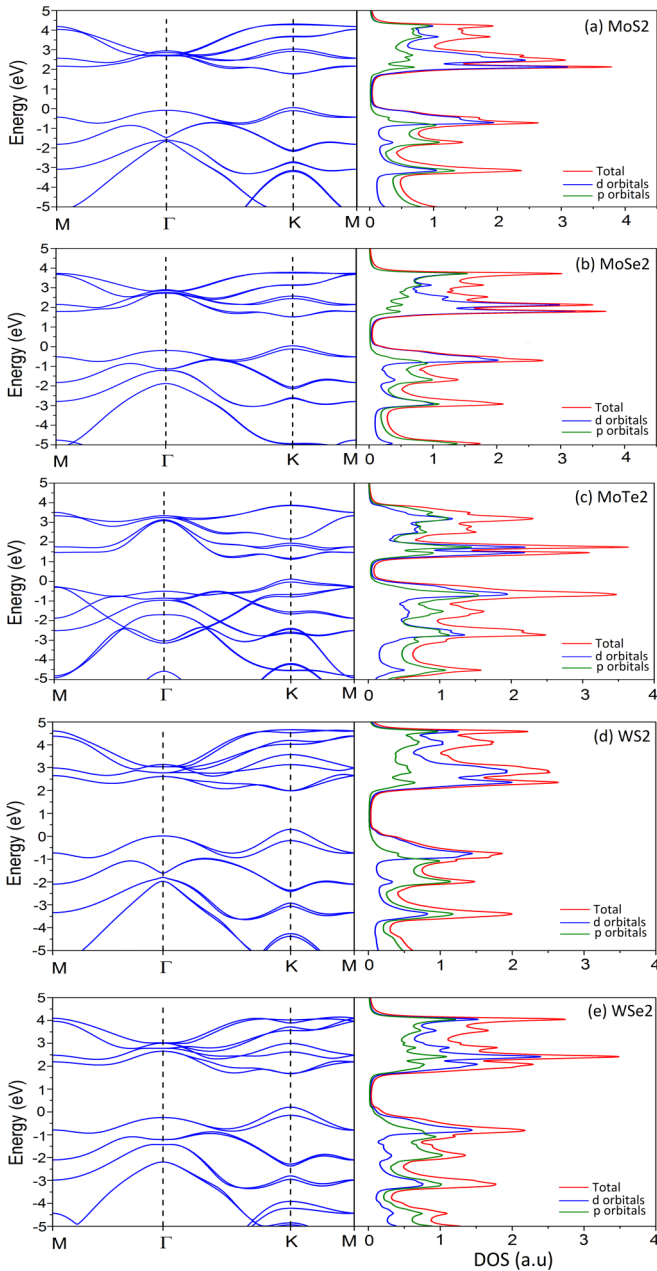
FIG. 8. Band structure along the path M-Γ-K-M (left-hand side) and corresponding density of states (DOS) (right-hand side) of the monolayer MoS_2 (a), $MoSe_2$ (b), $MoTe_2$ (c), WS_2 (d), and WSe_2 (e), respectively, with spin-orbit coupling, obtained by TB calculation. The green and blue curves correspond to the DOSs stemmed from p and d orbitals, respectively. The red one represents the total DOS.

(see V_1), both spins circulate in the same direction, therefore the system is actually in a quantum valley Hall (QVH) phase (for each spin), protected by the time-reversal symmetry. It is closely analogous to the spin Hall effect with the spin-polarized electrons replaced by valley-polarized carriers [2,6,45]. The underlying physics can be understood as follows. Because of the broken inversion symmetry in its crystal structure and strong SOC, the MoS_2 possesses two degenerate valleys, with equal and opposite Berry curvature. Hence, electrons in the two valleys experience effective magnetic fields which are

proportional to the Berry curvature with equal magnitude but opposite sign [6,46]. As a result, electrons from different valleys feel opposite Lorentz-type forces and move in opposite directions perpendicular to the drift current, resulting in QVH. Since the QVH originates from the coupling of the valley pseudospin to the orbital motion of the electrons, its existence is determined by physical parameters of the TMDC materials. We also notice that for a given Fermi level (0.875 meV), only the MoS_2 NR presents the QVH.

In Fig. 11, we show the electronic structure of TMDC armchair NRs with a width defined by $n_{max} = 200$. Because of the spin degeneracy, only spin-up component is plotted. The edge states within band gap are *also* observed. Their position and shape depend on material. Unlike the zigzag NRs, the armchair NRs present the gapped spectrum of the edge modes. It arises from a combination of the effects of q^2 mass term in the continuum $k \cdot p$ model and a hybridization between one-dimensional modes on two edges of the ribbon [47–49]. This hybridization can be also understood in terms of a mixing of one-dimensional valleys (1D Dirac cones) on the edges [39]. For wide armchair NRs, the hybridization of these states on the different edges is weak, then the gap of the edge modes decreases.

IV. CONCLUSION

TB models exploited in calculating band structure of TMDCs contain two groups: one is based on group theory and the other uses SK two-center approximation, respectively. The former is computationally efficient, but not flexible to be extended to confined finite systems with lower symmetry such as disordered systems, quantum dots, and NRs. In contrast, the latter usually has high flexibility, but the accuracy of its outcome is not desirable, especially for the energy bands away from the Fermi level. Here, we present an improved scheme of the flexible SK TB method in which the second-nearest-neighbor M-M and X-X hopping terms are included. Its improvement, being of comparable accuracy to first-principles calculations, is clearly elucidated through a comprehensive comparison between our results and those produced by widely accepted TB models in literature for monolayer MoS_2. We afford transferable SK parameters including spin-orbit interaction strength for five different MX_2 (M = Mo, W; X = S, Se, Te), which allows readers who require high-precision TB outcome to implement their own TB model straightforwardly. In addition, we have employed our TB model to explore the electronic structures and topological aspects of the five-monolayer TMDC NRs. Finally, it is worth to remark that our improved TB model not only can provide reliable band structure of the monolayer TMDCs and their NRs, but also can be easily applied to the other 2D materials and extended to van der Waals heterostructures, quantum dots, nanotubes, the 2D materials with vacancy defects, and strain effect, etc.
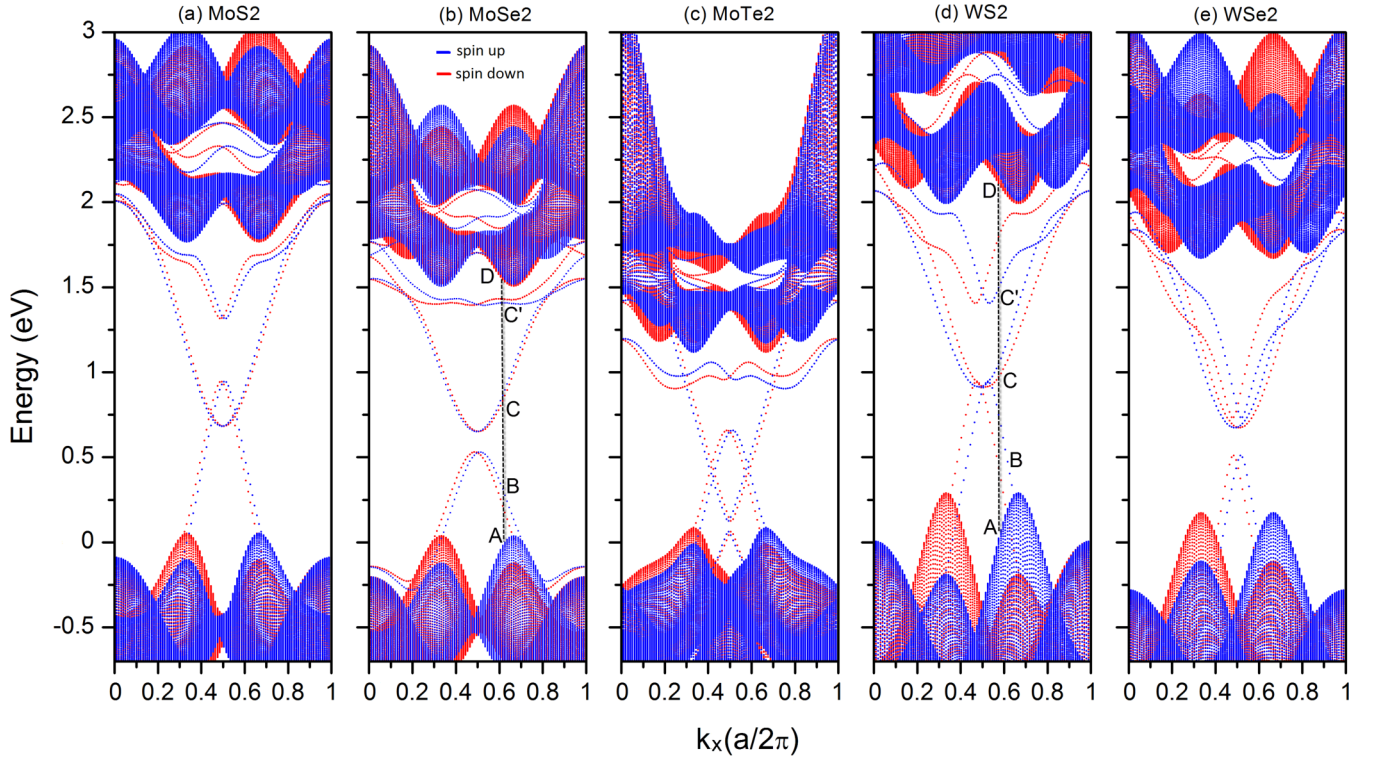
FIG. 9. Band structures of zigzag MoS_2 (a), $MoSe_2$ (b), $MoTe_2$ (c), WS_2 (d), and WSe_2 (e) NRs along the x axis whose width is defined by $n_{max} = 200$ along the y direction. The blue and red curves correspond to the spin-up and -down states, respectively. A, B, C, C′, and D are the crossing points of dashed vertical line with the NR energy bands. The two inequivalent valleys K and K' are located at $k_x a/(2\pi) = \frac{1}{3}$ and $\frac{2}{3}$, respectively, and a is the bulk's lattice constant.

APPENDIX A: MATRIX ELEMENTS OF THE TB HAMILTONIAN WITHOUT SOC

In this appendix, we show the matrix elements of the TB Hamiltonian in the absence of SOC, which are listed below. As we intend to list all matrix elements for our improved TB model and the number of equations is large, the equations of the same kind are group numbered in all appendices from A–D, instead of being numbered one by one, for convenience of differentiation.

$$M^E = \begin{pmatrix} E_{d_0}^e & 0 & 0 \\ 0 & E_{d_1}^e & 0 \\ 0 & 0 & E_{d_1}^e \end{pmatrix}, \quad M^O = \begin{pmatrix} E_{d_2}^o & 0 \\ 0 & E_{d_2}^o \end{pmatrix},$$

$$X^E = \begin{pmatrix} E_{s_2}^e & 0 & 0 \\ 0 & E_{s_1}^e & 0 \\ 0 & 0 & E_{s_1}^e \end{pmatrix}, \quad X^O = \begin{pmatrix} E_{s_2}^o & 0 & 0 \\ 0 & E_{s_1}^o & 0 \\ 0 & 0 & E_{s_1}^o \end{pmatrix},$$

$$\text{(A1)}$$

where $E_{d_0}^e$, $E_{d_1}^e$, $E_{d_2}^o$ are onsite energies of d_{z^2}, d_{xy} ($d_{x^2-y^2}$) and d_{xz} (d_{yz}) orbitals of M atom, respectively:

$$H_{M\text{-}X}^{E/O} = \sum_{i=1}^{3} e^{i\vec{k}\cdot\vec{A}_i} H_{M\text{-}X}^{E/O}(\vec{A}_i),$$

$$H_{M\text{-}M}^{E/O} = \sum_{i=1}^{6} e^{i\vec{k}\cdot\vec{S}_i} H_M^{E/O}(\vec{S}_i) + \sum_{i=1}^{6} e^{i\vec{k}\cdot\vec{C}_i} H_M^{E/O}(\vec{C}_i),$$

$$H_{X\text{-}X}^{E/O} = H_{tb}^{E/O} + \sum_{i=1}^{6} e^{i\vec{k}\cdot\vec{S}_i} H_X^{E/O}(\vec{S}_i)$$

$$+ \sum_{i=1}^{6} e^{i\vec{k}\cdot\vec{C}_i} H_X^{E/O}(\vec{C}_i), \quad \text{(A2)}$$

with the tb index indicating the intralayer X-X hopping in the top and bottom layers and the hopping vectors $\vec{A}_i$ ($i = 1, \ldots, 3$), $\vec{S}_j$, and $\vec{C}_j$ ($j = 1, \ldots, 6$) being given in Table II. The involving even and odd hopping matrices are defined as follows.

The even hopping matrices are written as

$$H_{M\text{-}X}^E(\vec{A}_1) = \begin{pmatrix} \sqrt{2}k_2 & 0 & 2\sqrt{2}k_1 \\ 0 & \sqrt{2}k_3 & 0 \\ 2\sqrt{2}k_{10} & 0 & \sqrt{2}k_8 \end{pmatrix},$$

$$H_{M\text{-}X}^E(\vec{A}_2) = \begin{pmatrix} \sqrt{2}k_2 & \sqrt{2}k_0 & -\sqrt{2}k_1 \\ \sqrt{2}k_6 & \sqrt{2}k_4 & \sqrt{2}k_5 \\ -\sqrt{2}k_{10} & \sqrt{2}k_7 & \sqrt{2}k_9 \end{pmatrix},$$

$$H_{M\text{-}X}^E(\vec{A}_3) = \begin{pmatrix} \sqrt{2}k_2 & -\sqrt{2}k_0 & -\sqrt{2}k_1 \\ -\sqrt{2}k_6 & \sqrt{2}k_4 & -\sqrt{2}k_5 \\ -\sqrt{2}k_{10} & -\sqrt{2}k_7 & \sqrt{2}k_9 \end{pmatrix},$$

$$H_M^E(\vec{S}_1) = \begin{pmatrix} t_0 & 0 & -2t_2 \\ 0 & t_3 & 0 \\ -2t_2 & 0 & t_6 \end{pmatrix} = H_M^E(\vec{S}_4),$$
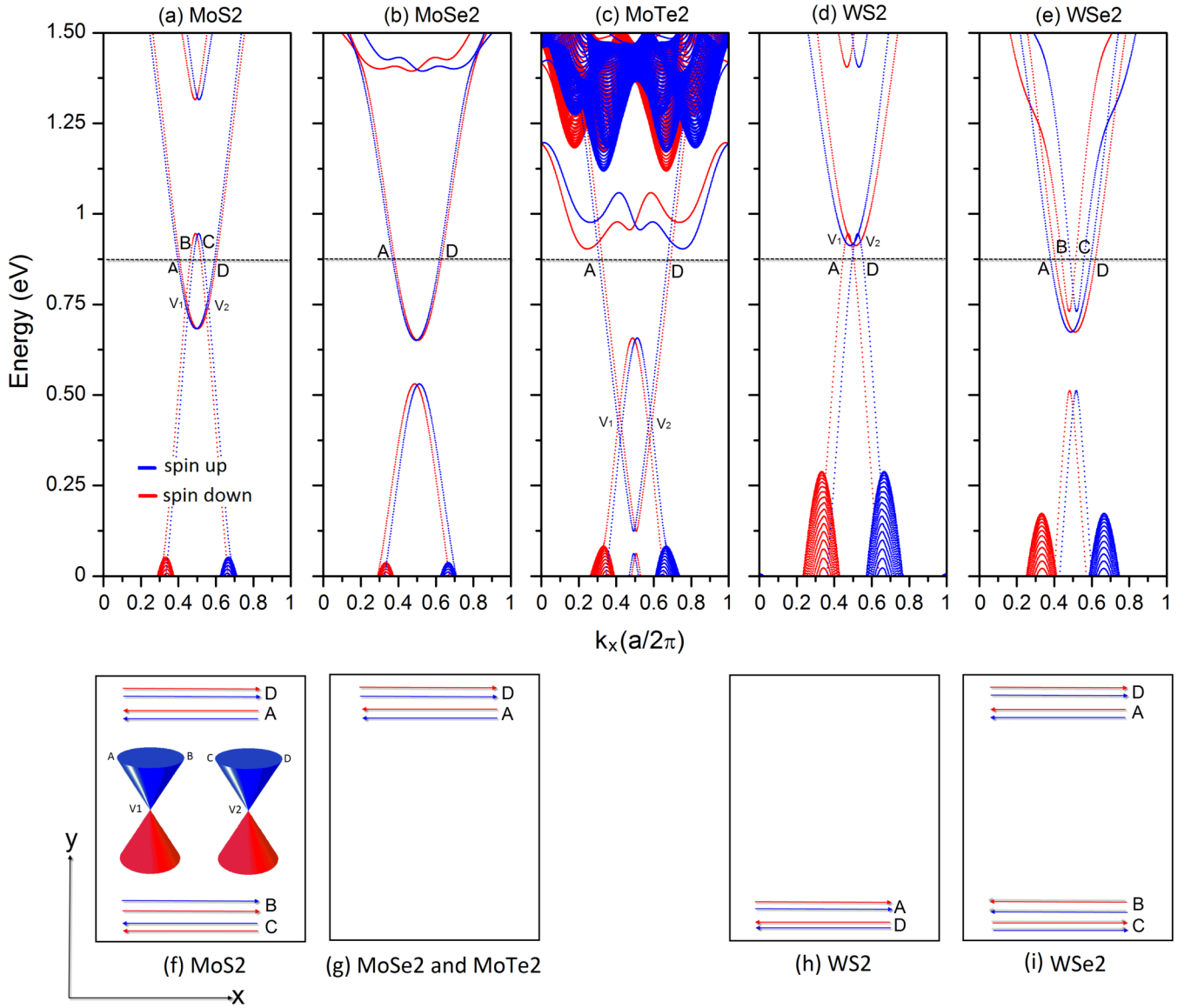
FIG. 10. Upper panels: zoom of the edge states in zigzag nanorribons along the x axis and whose width is defined by $n_{max} = 200$ along the y direction for (a) MoS_2, (b) $MoSe_2$, (c) $MoTe_2$, (d) WS_2, and (e) WSe_2, respectively, shown in Fig. 9. The blue and red curves correspond to the spin-up and -down states, respectively. The dashed horizontal line indicates assumed Fermi level. A, B, C, and D are the crossing points of Fermi level with the NR energy bands. a is the bulk's lattice constant. The lower panels are schematics of the locations of the edge states A, B, C, and D. The arrows indicate directions of the velocity. The red and blue lines correspond to the spin-up and -down states, respectively.

$$H_M^E(\vec{S}_2) = \begin{pmatrix} t_0 & t_1 & t_2 \\ t_1 & t_4 & t_5 \\ t_2 & t_5 & t_7 \end{pmatrix} = H_M^E(\vec{S}_5),$$

$$H_X^E(\vec{S}_2) = \begin{pmatrix} p_3^e & 0 & 0 \\ 0 & p_1^e & p_2^e \\ 0 & p_2^e & p_4^e \end{pmatrix} = H_X^E(\vec{S}_5),$$

$$H_M^E(\vec{S}_3) = \begin{pmatrix} t_0 & -t_1 & t_2 \\ -t_1 & t_4 & -t_5 \\ t_2 & -t_5 & t_7 \end{pmatrix} = H_M^E(\vec{S}_6),$$

$$H_X^E(\vec{S}_3) = \begin{pmatrix} p_3^e & 0 & 0 \\ 0 & p_1^e & -p_2^e \\ 0 & -p_2^e & p_4^e \end{pmatrix} = H_X^E(\vec{S}_6),$$

$$H_X^E(\vec{S}_1) = \begin{pmatrix} p_3^e & 0 & 0 \\ 0 & p_0^e & 0 \\ 0 & 0 & p_3^e \end{pmatrix} = H_X^E(\vec{S}_4),$$

$$H_M^E(\vec{C}_1) = \begin{pmatrix} u_0 & u_1 & u_2 \\ u_1 & u_4 & u_6 \\ u_2 & u_6 & u_7 \end{pmatrix} = H_M^E(\vec{C}_4),$$

$$H_M^E(\vec{C}_2) = \begin{pmatrix} u_0 & 0 & u_3 \\ 0 & u_5 & 0 \\ u_3 & 0 & u_8 \end{pmatrix} = H_M^E(\vec{C}_5),$$

$$H_M^E(\vec{C}_3) = \begin{pmatrix} u_0 & -u_1 & u_2 \\ -u_1 & u_4 & -u_6 \\ u_2 & -u_6 & u_7 \end{pmatrix} = H_M^E(\vec{C}_6),$$

$$H_X^E(\vec{C}_1) = \begin{pmatrix} q_1^e & 0 & 0 \\ 0 & q_0^e & q_2^e \\ 0 & q_2^e & q_3^e \end{pmatrix} = H_X^E(\vec{C}_4),$$

$$H_X^E(\vec{C}_2) = \begin{pmatrix} q_1^e & 0 & 0 \\ 0 & q_1^e & 0 \\ 0 & 0 & q_4^e \end{pmatrix} = H_X^E(\vec{C}_5),$$

$$H_X^E(\vec{C}_3) = \begin{pmatrix} q_1^e & 0 & 0 \\ 0 & q_0^e & -q_2^e \\ 0 & -q_2^e & q_3^e \end{pmatrix} = H_X^E(\vec{C}_6),$$

$$H_{tb}^E = \begin{pmatrix} -h_2^e & 0 & 0 \\ 0 & h_1^e & 0 \\ 0 & 0 & h_1^e \end{pmatrix}. \tag{A3}$$

The odd hopping matrices read as

$$H_{M\text{-}X}^O(\vec{A}_1) = \begin{pmatrix} 0 & \sqrt{2}k_{15} & 0 \\ -2\sqrt{2}k_{14} & 0 & \sqrt{2}k_{12} \end{pmatrix},$$

$$H_{M\text{-}X}^O(\vec{A}_2) = \begin{pmatrix} \sqrt{2}k_{18} & \sqrt{2}k_{16} & \sqrt{2}k_{17} \\ \sqrt{2}k_{14} & \sqrt{2}k_{11} & \sqrt{2}k_{13} \end{pmatrix},$$

$$H_{M\text{-}X}^O(\vec{A}_3) = \begin{pmatrix} -\sqrt{2}k_{18} & \sqrt{2}k_{16} & -\sqrt{2}k_{17} \\ \sqrt{2}k_{14} & -\sqrt{2}k_{11} & \sqrt{2}k_{13} \end{pmatrix},$$

$$H_M^O(\vec{S}_1) = \begin{pmatrix} t_{11} & 0 \\ 0 & t_8 \end{pmatrix} = H_M^O(\vec{S}_4),$$

$$H_M^O(\vec{S}_2) = \begin{pmatrix} t_{12} & t_{10} \\ t_{10} & t_9 \end{pmatrix} = H_M^O(\vec{S}_5),$$

$$H_M^O(\vec{S}_3) = \begin{pmatrix} t_{12} & -t_{10} \\ -t_{10} & t_9 \end{pmatrix} = H_M^O(\vec{S}_6),$$

$$H_X^O(\vec{S}_1) = \begin{pmatrix} p_3^o & 0 & 0 \\ 0 & p_0^o & 0 \\ 0 & 0 & p_3^o \end{pmatrix} = H_X^O(\vec{S}_4),$$

$$H_X^O(\vec{S}_2) = \begin{pmatrix} p_3^o & 0 & 0 \\ 0 & p_1^o & p_2^o \\ 0 & p_2^o & p_4^o \end{pmatrix} = H_X^O(\vec{S}_5),$$

$$H_X^O(\vec{S}_3) = \begin{pmatrix} p_3^o & 0 & 0 \\ 0 & p_1^o & -p_2^o \\ 0 & -p_2^o & p_4^o \end{pmatrix} = H_X^O(\vec{S}_6),$$

$$H_M^O(\vec{C}_1) = \begin{pmatrix} u_{12} & u_{11} \\ u_{11} & u_9 \end{pmatrix} = H_M^O(\vec{C}_4),$$

$$H_M^O(\vec{C}_2) = \begin{pmatrix} u_{13} & 0 \\ 0 & u_{10} \end{pmatrix} = H_M^O(\vec{C}_5),$$

$$H_M^O(\vec{C}_3) = \begin{pmatrix} u_{12} & -u_{11} \\ -u_{11} & u_9 \end{pmatrix} = H_M^O(\vec{C}_6),$$

$$H_X^O(\vec{C}_1) = \begin{pmatrix} q_1^o & 0 & 0 \\ 0 & q_0^o & q_2^o \\ 0 & q_2^o & q_3^o \end{pmatrix} = H_X^O(\vec{C}_4),$$

$$H_X^O(\vec{C}_2) = \begin{pmatrix} q_1^o & 0 & 0 \\ 0 & q_1^o & 0 \\ 0 & 0 & q_4^o \end{pmatrix} = H_X^O(\vec{C}_5),$$

$$H_X^O(\vec{C}_3) = \begin{pmatrix} q_1^o & 0 & 0 \\ 0 & q_0^o & -q_2^o \\ 0 & -q_2^o & q_3^o \end{pmatrix} = H_X^O(\vec{C}_6),$$

$$H_{tb}^O = \begin{pmatrix} h_2^o & 0 & 0 \\ 0 & -h_1^o & 0 \\ 0 & 0 & -h_1^o \end{pmatrix}. \tag{A4}$$

In Eqs. (A3) and (A4), k, t, p, u, q, and h are the hopping parameters defined in terms of the SK parameters (see Tables VI and VII). The corresponding expressions of the hopping parameters under the two-center approximation based on a definition using the SK method shown in Tables VI and VII, are listed below, with

$$k_0 = \frac{3}{2} V_{pd\pi}^e \cos\theta \sin^2\theta$$
$$- \frac{\sqrt{3}}{2} V_{pd\sigma}^e \cos\theta \left(\sin^2\theta - \frac{1}{2}\cos^2\theta \right),$$

$$k_1 = -\frac{\sqrt{3}}{2} V_{pd\pi}^e \cos\theta \sin^2\theta$$
$$+ \frac{1}{2} V_{pd\sigma}^e \cos\theta \left(\sin^2\theta - \frac{1}{2}\cos^2\theta \right),$$

$$k_2 = \sqrt{3}\, V_{pd\pi}^e \cos^2\theta \sin\theta + V_{pd\sigma}^e \cos\theta \left(\sin^2\theta - \frac{1}{2}\cos^2\theta \right),$$

$$k_3 = V_{pd\pi}^e \cos\theta,$$

$$k_4 = -\frac{3\sqrt{3}}{8} V_{pd\sigma}^e \cos^3\theta - \frac{1}{2} V_{pd\pi}^e \cos\theta \left(1 - \frac{3}{2}\cos^2\theta \right),$$

$$k_5 = -\frac{3}{8} V_{pd\sigma}^e \cos^3\theta - \frac{\sqrt{3}}{2} V_{pd\pi}^e \cos\theta \left(1 - \frac{1}{2}\cos^2\theta \right),$$
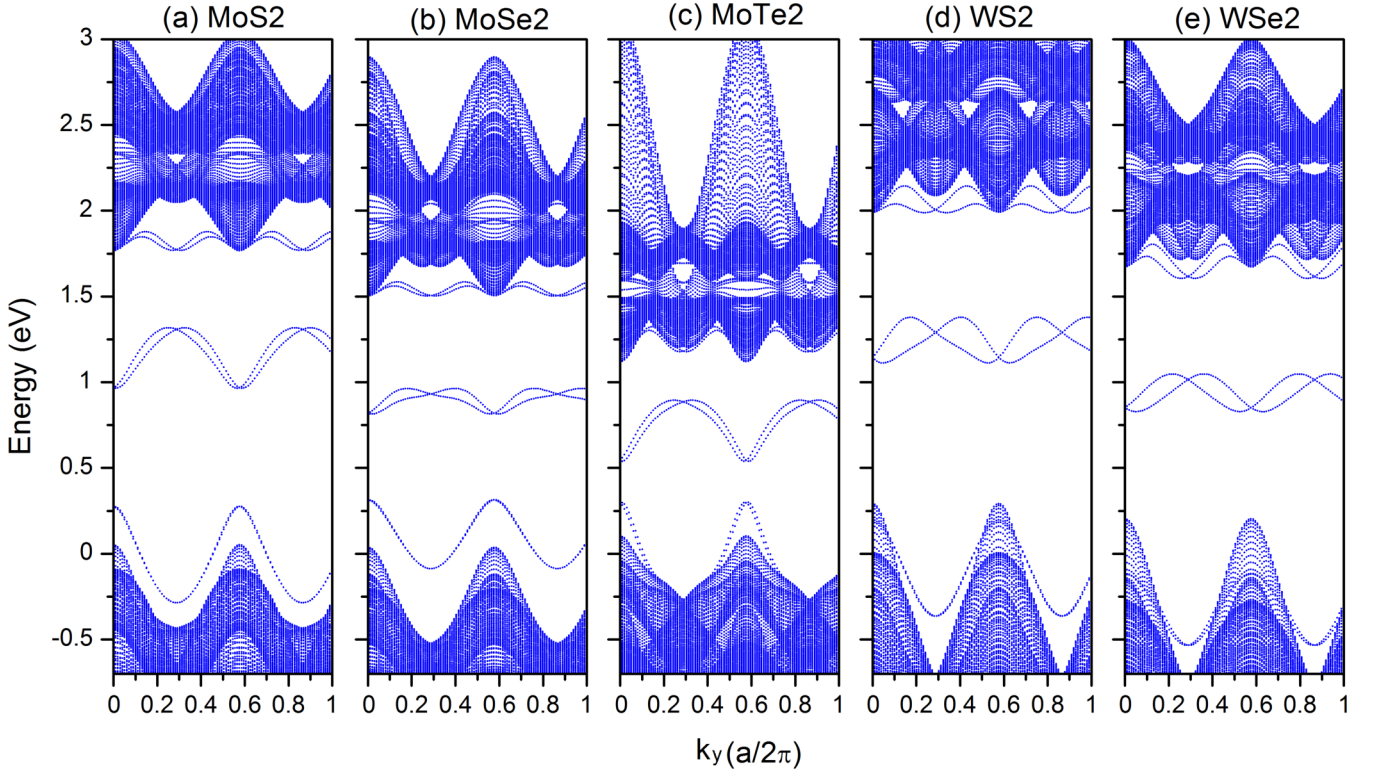
FIG. 11. Band structures of armchair NRs along the y axis whose width is defined by $n_{max} = 200$ along the x direction for (a) MoS$_2$, (b) MoSe$_2$, (c) MoTe$_2$, (d) WS$_2$, and (e) WSe$_2$, respectively. The two inequivalent valleys K and K' are located at $k_x a/(2\pi) = \frac{1}{3}$ and $\frac{2}{3}$, respectively. a is the bulk's lattice constant. Owing to the spin degeneracy in the armchair NRs, only spin-up component is plotted.

$$k_6 = -\frac{\sqrt{3}}{2} V^e_{pd\pi} \cos^2\theta \, \sin\theta + \frac{3}{4} V^e_{pd\sigma} \cos^2\theta \, \sin\theta,$$

$$k_7 = k_5,$$

$$k_8 = -\frac{\sqrt{3}}{2} \cos^3\theta \, V^e_{pd\sigma} - \cos\theta \, \sin^2\theta \, V^e_{pd\pi},$$

$$k_9 = -\frac{\sqrt{3}}{8} \cos^3\theta \, V^e_{pd\sigma} + \frac{1}{2} V^e_{pd\pi} \cos\theta \left(1 + \frac{1}{2}\cos^2\theta\right),$$

$$k_{10} = \frac{1}{2} V^e_{pd\pi} \cos^2\theta \, \sin\theta - \frac{\sqrt{3}}{4} V^e_{pd\sigma} \cos^2\theta \, \sin\theta,$$

$$k_{11} = -\frac{\sqrt{3}}{2} V^o_{pd\pi} \cos^2\theta \, \sin\theta + \frac{3}{4} V^o_{pd\sigma} \cos^2\theta \, \sin\theta,$$

$$k_{12} = \sqrt{3} V^o_{pd\sigma} \cos^2\theta \, \sin\theta + V^o_{pd\pi}(1 - 2\cos^2\theta) \, \sin\theta,$$

$$k_{13} = \frac{\sqrt{3}}{4} V^o_{pd\sigma} \cos^2\theta \, \sin\theta + V^o_{pd\pi}\left(1 - \frac{1}{2}\cos^2\theta\right) \sin\theta,$$

$$k_{14} = -\frac{\sqrt{3}}{2} V^o_{pd\sigma} \sin^2\theta \, \cos\theta - \frac{1}{2} V^o_{pd\pi}(1 - 2\sin^2\theta) \, \cos\theta,$$

$$k_{15} = V^o_{pd\pi} \sin\theta,$$

$$k_{16} = \frac{3\sqrt{3}}{4} V^o_{pd\sigma} \cos^2\theta \, \sin\theta + V^o_{pd\pi}\left(1 - \frac{3}{2}\cos^2\theta\right) \sin\theta,$$

$$k_{17} = -\frac{\sqrt{3}}{2} V^o_{pd\pi} \cos^2\theta \, \sin\theta + \frac{3}{4} V^o_{pd\sigma} \cos^2\theta \, \sin\theta,$$

$$k_{18} = -\frac{3}{2} V^o_{pd\sigma} \sin^2\theta \, \cos\theta - \frac{\sqrt{3}}{2} V^o_{pd\pi}(1 - 2\sin^2\theta) \, \cos\theta, \qquad (A5)$$

$$t_0 = \frac{3}{4} V^e_{dd\delta} + \frac{1}{4} V^e_{dd\sigma},$$

$$t_1 = \frac{3}{8} V^e_{dd\delta} - \frac{3}{8} V^e_{dd\sigma},$$

$$t_2 = -\frac{\sqrt{3}}{8} V^e_{dd\delta} + \frac{\sqrt{3}}{8} V^e_{dd\sigma},$$

$$t_3 = V_{dd\pi}^e,$$

$$t_4 = \frac{3}{16} V_{dd\delta}^e + \frac{1}{4} V_{dd\pi}^e + \frac{9}{16} V_{dd\sigma}^e,$$

$$t_5 = -\frac{\sqrt{3}}{16} V_{dd\delta}^e + \frac{\sqrt{3}}{4} V_{dd\pi}^e - \frac{3\sqrt{3}}{16} V_{dd\sigma}^e,$$

$$t_6 = \frac{1}{4} V_{dd\delta}^e + \frac{3}{4} V_{dd\sigma}^e,$$

$$t_7 = \frac{1}{16} V_{dd\delta}^e + \frac{3}{4} V_{dd\pi}^e + \frac{3}{16} V_{dd\sigma}^e,$$

$$t_8 = V_{dd\delta}^o,$$

$$t_9 = \frac{1}{4} V_{dd\delta}^o + \frac{3}{4} V_{dd\pi}^o,$$

$$t_{10} = -\frac{\sqrt{3}}{4} V_{dd\delta}^o + \frac{\sqrt{3}}{4} V_{dd\pi}^o,$$

$$t_{11} = V_{dd\pi}^o,$$

$$t_{12} = \frac{3}{4} V_{dd\delta}^o + \frac{1}{4} V_{dd\pi}^o, \tag{A6}$$

$$p_0^{e/o} = V_{pp\sigma}^{e/o},$$

$$p_1^{e/o} = \frac{3}{4} V_{pp\pi}^{e/o} + \frac{1}{4} V_{pp\sigma}^{e/o},$$

$$p_2^{e/o} = \frac{-\sqrt{3}}{4} V_{pp\pi}^{e/o} + \frac{\sqrt{3}}{4} V_{pp\sigma}^{e/o},$$

$$p_3^{e/o} = V_{pp\pi}^{e/o},$$

$$p_4^{e/o} = \frac{1}{4} V_{pp\pi}^{e/o} + \frac{3}{4} V_{pp\sigma}^{e/o}, \tag{A7}$$

$$u_0 = \frac{3}{4} K_{dd\delta}^e + \frac{1}{4} K_{dd\sigma}^e,$$

$$u_1 = \frac{3}{8} K_{dd\delta}^e - \frac{3}{8} K_{dd\sigma}^e,$$

$$u_2 = \frac{\sqrt{3}}{8} K_{dd\delta}^e - \frac{\sqrt{3}}{8} K_{dd\sigma}^e,$$

$$u_3 = -\frac{\sqrt{3}}{4} K_{dd\delta}^e + \frac{\sqrt{3}}{4} K_{dd\sigma}^e,$$

$$u_4 = \frac{3}{16} K_{dd\delta}^e + \frac{1}{4} K_{dd\pi}^e + \frac{9}{16} K_{dd\sigma}^e,$$

$$u_5 = K_{dd\pi}^e,$$

$$u_6 = \frac{\sqrt{3}}{16} K_{dd\delta}^e - \frac{\sqrt{3}}{4} K_{dd\pi}^e + \frac{3\sqrt{3}}{16} K_{dd\sigma}^e,$$

$$u_7 = \frac{1}{16} K_{dd\delta}^e + \frac{3}{4} K_{dd\pi}^e + \frac{3}{16} K_{dd\sigma}^e,$$

$$u_8 = \frac{1}{4} K_{dd\delta}^e + \frac{3}{4} K_{dd\sigma}^e,$$

$$u_9 = \frac{3}{4} K_{dd\delta}^o + \frac{1}{4} K_{dd\pi}^o,$$

$$u_{10} = K_{dd\pi}^o,$$

$$u_{11} = -\frac{\sqrt{3}}{4} K_{dd\delta}^o + \frac{\sqrt{3}}{4} K_{dd\pi}^o,$$

$$u_{12} = \frac{1}{4} K_{dd\delta}^o + \frac{3}{4} K_{dd\pi}^o,$$

$$u_{13} = K_{dd\delta}^o, \tag{A8}$$

$$q_0^{e/o} = \frac{1}{4} K_{pp\pi}^{e/o} + \frac{3}{4} K_{pp\sigma}^{e/o},$$

$$q_1^{e/o} = K_{pp\pi}^{e/o},$$

$$q_2^{e/o} = -\frac{\sqrt{3}}{4} K_{pp\pi}^{e/o} + \frac{\sqrt{3}}{4} K_{pp\sigma}^{e/o},$$

$$q_3^{e/o} = \frac{3}{4} K_{pp\pi}^{e/o} + \frac{1}{4} K_{pp\sigma}^{e/o},$$

$$q_4^{e/o} = K_{pp\sigma}^{e/o}, \tag{A9}$$

$$h_1^{e/o} = V_{pp\pi}^{e/o},$$

$$h_2^{e/o} = V_{pp\sigma}^{e/o}. \tag{A10}$$

APPENDIX B: SOC MATRICES OF THE TB HAMILTONIAN

In this appendix, we show the SOC matrices for the TB Hamiltonian, which are written as

$$H_{\mathrm{SO1}}^{\uparrow\uparrow} = \begin{pmatrix} 0 & 0 & 0 & 0 & 0 & 0 \\ 0 & 0 & i\lambda_M & 0 & 0 & 0 \\ 0 & -i\lambda_M & 0 & 0 & 0 & 0 \\ 0 & 0 & 0 & 0 & 0 & 0 \\ 0 & 0 & 0 & 0 & 0 & -\frac{i}{2}\lambda_X \\ 0 & 0 & 0 & 0 & \frac{i}{2}\lambda_X & 0 \end{pmatrix},$$

$$H_{\mathrm{SO2}}^{\uparrow\uparrow} = \begin{pmatrix} 0 & -\frac{i}{2}\lambda_M & 0 & 0 & 0 \\ \frac{i}{2}\lambda_M & 0 & 0 & 0 & 0 \\ 0 & 0 & 0 & 0 & 0 \\ 0 & 0 & 0 & 0 & -\frac{i}{2}\lambda_X \\ 0 & 0 & 0 & \frac{i}{2}\lambda_X & 0 \end{pmatrix},$$

$$H_{\text{SO1}}^{\uparrow\downarrow} = \begin{pmatrix} -\frac{\sqrt{3}}{2}\lambda_M & i\frac{\sqrt{3}}{2}\lambda_M & 0 & 0 & 0 \\ -i\frac{\lambda_M}{2} & \frac{\lambda_M}{2} & 0 & 0 & 0 \\ \frac{\lambda_M}{2} & i\frac{\lambda_M}{2} & 0 & 0 & 0 \\ 0 & 0 & 0 & -\frac{\lambda_X}{2} & i\frac{\lambda_X}{2} \\ 0 & 0 & \frac{\lambda_X}{2} & 0 & 0 \\ 0 & 0 & -i\frac{\lambda_X}{2} & 0 & 0 \end{pmatrix},$$

$$H_{\text{SO2}}^{\uparrow\downarrow} = \begin{pmatrix} \frac{\sqrt{3}}{2}\lambda_M & i\frac{\lambda_M}{2} & -\frac{\lambda_M}{2} & 0 & 0 & 0 \\ -i\frac{\sqrt{3}\lambda_M}{2} & -\frac{\lambda_M}{2} & -i\frac{\lambda_M}{2} & 0 & 0 & 0 \\ 0 & 0 & 0 & 0 & -\frac{\lambda_X}{2} & i\frac{\lambda_X}{2} \\ 0 & 0 & 0 & \frac{\lambda_X}{2} & 0 & 0 \\ 0 & 0 & 0 & -i\frac{\lambda_X}{2} & 0 & 0 \end{pmatrix},$$

$$H_{\text{SO1}}^{\downarrow\uparrow} = \begin{pmatrix} \frac{\sqrt{3}}{2}\lambda_M & i\frac{\sqrt{3}}{2}\lambda_M & 0 & 0 & 0 \\ -i\frac{\lambda_M}{2} & -\frac{\lambda_M}{2} & 0 & 0 & 0 \\ -\frac{\lambda_M}{2} & i\frac{\lambda_M}{2} & 0 & 0 & 0 \\ 0 & 0 & 0 & \frac{\lambda_X}{2} & i\frac{\lambda_X}{2} \\ 0 & 0 & -\frac{\lambda_X}{2} & 0 & 0 \\ 0 & 0 & -i\frac{\lambda_X}{2} & 0 & 0 \end{pmatrix},$$

$$H_{\text{SO2}}^{\downarrow\uparrow} = \begin{pmatrix} -\frac{\sqrt{3}}{2}\lambda_M & i\frac{\lambda_M}{2} & \frac{\lambda_M}{2} & 0 & 0 & 0 \\ -i\frac{\sqrt{3}\lambda_M}{2} & \frac{\lambda_M}{2} & -i\frac{\lambda_M}{2} & 0 & 0 & 0 \\ 0 & 0 & 0 & 0 & \frac{\lambda_X}{2} & i\frac{\lambda_X}{2} \\ 0 & 0 & 0 & -\frac{\lambda_X}{2} & 0 & 0 \\ 0 & 0 & 0 & -i\frac{\lambda_X}{2} & 0 & 0 \end{pmatrix},$$

$$H_{\text{SO1}}^{\downarrow\downarrow} = \begin{pmatrix} 0 & 0 & 0 & 0 & 0 & 0 \\ 0 & 0 & -i\lambda_M & 0 & 0 & 0 \\ 0 & i\lambda_M & 0 & 0 & 0 & 0 \\ 0 & 0 & 0 & 0 & 0 & 0 \\ 0 & 0 & 0 & 0 & 0 & \frac{i}{2}\lambda_X \\ 0 & 0 & 0 & 0 & -\frac{i}{2}\lambda_X & 0 \end{pmatrix},$$

$$H_{\text{SO2}}^{\downarrow\downarrow} = \begin{pmatrix} 0 & \frac{i}{2}\lambda_M & 0 & 0 & 0 \\ -\frac{i}{2}\lambda_M & 0 & 0 & 0 & 0 \\ 0 & 0 & 0 & 0 & 0 \\ 0 & 0 & 0 & 0 & \frac{i}{2}\lambda_X \\ 0 & 0 & 0 & -\frac{i}{2}\lambda_X & 0 \end{pmatrix}, \quad \text{(B1)}$$

where λ_M and λ_X stand for the SOC strength for M and X atoms, respectively.

APPENDIX C: TB MATRIX ELEMENTS FOR ZIGZAG NANORIBBONS

In this appendix, we show the matrix elements of the TB Hamiltonian for zigzag nanoribbons:

$$M^{ZZ}(\tau) = \left(M^E + \tau H_M^{\text{SOC}} \right)|m, n\rangle\langle m, n|,$$

$$X^{ZZ}(\tau) = \left(X^E + H_{tb}^E + \tau H_X^{\text{SOC}} \right)|m, n\rangle\langle m, n|, \quad \text{(C1)}$$

with

$$H_M^{\text{SOC}} = \begin{pmatrix} 0 & 0 & 0 \\ 0 & 0 & i\lambda_M \\ 0 & -i\lambda_M & 0 \end{pmatrix},$$

$$H_X^{\text{SOC}} = \begin{pmatrix} 0 & 0 & 0 \\ 0 & 0 & -i\frac{\lambda_X}{2} \\ 0 & i\frac{\lambda_X}{2} & 0 \end{pmatrix}. \quad \text{(C2)}$$

$$\begin{aligned} H_{M\text{-}M}^{ZZ} &= H_{M1}^{ZZ}|m, n\rangle\langle m, n| + H_{M4}^{ZZ}|m, n\rangle\langle m, n+4| \\ &\quad + H_{M2}^{ZZ}(|m, n\rangle\langle m+1, n+2| \\ &\quad + |m, n\rangle\langle m-1, n+2|) \\ &\quad + H_{M3}^{ZZ}(|m, n\rangle\langle m+1, n-2| \\ &\quad + |m, n\rangle\langle m-1, n-2|) \\ &\quad + H_{M5}^{ZZ}|m, n\rangle\langle m, n-4|, \quad \text{(C3)} \end{aligned}$$

with

$$H_{M1}^{ZZ} = H_M^E(\vec{S}_1)e^{ik_x\vec{S}_1.\hat{x}} + H_M^E(\vec{S}_4)e^{ik_x\vec{S}_4.\hat{x}},$$

$$\begin{aligned} H_{M2}^{ZZ} &= H_M^E(\vec{S}_2)e^{ik_x\vec{S}_2.\hat{x}} + H_M^E(\vec{S}_3)e^{ik_x\vec{S}_3.\hat{x}} \\ &\quad + H_M^E(\vec{C}_1)e^{ik_x\vec{C}_1.\hat{x}} + H_M^E(\vec{C}_3)e^{ik_x\vec{C}_3.\hat{x}}, \end{aligned}$$

$$\begin{aligned} H_{M3}^{ZZ} &= H_M^E(\vec{S}_5)e^{ik_x\vec{S}_5.\hat{x}} + H_M^E(\vec{S}_6)e^{ik_x\vec{S}_6.\hat{x}} \\ &\quad + H_M^E(\vec{C}_4)e^{ik_x\vec{C}_4.\hat{x}} + H_M^E(\vec{C}_6)e^{ik_x\vec{C}_6.\hat{x}}, \end{aligned}$$

$$H_{M4}^{ZZ} = H_M^E(\vec{C}_2)e^{ik_x\vec{C}_2.\hat{x}},$$

$$H_{M5}^{ZZ} = H_M^E(\vec{C}_5)e^{ik_x\vec{C}_5.\hat{x}}. \quad \text{(C4)}$$

$$\begin{aligned} H_{X\text{-}X}^{ZZ} &= H_{X1}^{ZZ}|m, n\rangle\langle m, n| + H_{X4}^{ZZ}|m, n\rangle\langle m, n+4| \\ &\quad + H_{X2}^{ZZ}(|m, n\rangle\langle m+1, n+2| + |m, n\rangle\langle m-1, n+2|) \\ &\quad + H_{X3}^{ZZ}(|m, n\rangle\langle m+1, n-2| + |m, n\rangle\langle m-1, n-2|) \\ &\quad + H_{X5}^{ZZ}|m, n\rangle\langle m, n-4|, \quad \text{(C5)} \end{aligned}$$

with

$$H_{X1}^{ZZ} = H_X^E(\vec{S}_1)e^{ik_x\vec{S}_1.\hat{x}} + H_X^E(\vec{S}_4)e^{ik_x\vec{S}_4.\hat{x}},$$

$$\begin{aligned} H_{X2}^{ZZ} &= H_X^E(\vec{S}_2)e^{ik_x\vec{S}_2.\hat{x}} + H_X^E(\vec{S}_3)e^{ik_x\vec{S}_3.\hat{x}} \\ &\quad + H_X^E(\vec{C}_1)e^{ik_x\vec{C}_1.\hat{x}} + H_X^E(\vec{C}_3)e^{ik_x\vec{C}_3.\hat{x}}, \end{aligned}$$

$$\begin{aligned} H_{X3}^{ZZ} &= H_X^E(\vec{S}_5)e^{ik_x\vec{S}_5.\hat{x}} + H_X^E(\vec{S}_6)e^{ik_x\vec{S}_6.\hat{x}} \\ &\quad + H_X^E(\vec{C}_4)e^{ik_x\vec{C}_4.\hat{x}} + H_X^E(\vec{C}_6)e^{ik_x\vec{C}_6.\hat{x}}, \end{aligned}$$

$$H_{X4}^{ZZ} = H_X^E(\vec{C}_2)e^{ik_x\vec{C}_2.\hat{x}},$$

$$H_{X5}^{ZZ} = H_X^E(\vec{C}_5)e^{ik_x\vec{C}_5.\hat{x}}, \quad \text{(C6)}$$

$$H_{M\text{-}X}^{ZZ} = H_{MX2}^{ZZ}|m,n\rangle\langle m-1,n-1|$$
$$+ H_{MX2}^{ZZ}|m,n\rangle\langle m+1,n-1|$$
$$+ H_{MX1}^{ZZ}|m,n\rangle\langle m,n+1|, \tag{C7}$$

$$H_{X\text{-}M}^{ZZ} = H_{MX2}^{ZZ\dagger}|m,n\rangle\langle m+1,n+1|$$
$$+ H_{MX2}^{ZZ\dagger}|m,n\rangle\langle m-1,n+1|$$
$$+ H_{MX1}^{ZZ\dagger}|m,n\rangle\langle m,n-1|, \tag{C8}$$

with

$$H_{MX1}^{ZZ} = H_{M-X}^E(\vec{A}_1)e^{ik_x\vec{A}_1.\hat{x}},$$

$$H_{MX2}^{ZZ} = H_{M-X}^E(\vec{A}_2)e^{ik_x\vec{A}_2.\hat{x}} + H_{M-X}^E(\vec{A}_3)e^{ik_x\vec{A}_3.\hat{x}}, \tag{C9}$$

where τ is the spin index, $\tau = 1$ (-1) corresponds to the spin-up (spin-down) states.

APPENDIX D: TB MATRIX ELEMENTS FOR ARMCHAIR NANORIBBONS

In this appendix, we show the matrix elements of the TB Hamiltonian for armchair nanoribbons:

$$M^{AC}(\tau) = \left(M^E + \tau H_M^{SOC}\right)|m,n\rangle\langle m,n|, \tag{D1}$$

$$X^{AC}(\tau) = \left(X^E + H_{tb}^E + \tau H_X^{SOC}\right)|m,n\rangle\langle m,n|. \tag{D2}$$

$$H_{M\text{-}M}^{AC}$$
$$= H_{M1}^{AC}|m,n\rangle\langle m,n| + H_{M2}^{AC}|m,n\rangle\langle m+2,n|$$
$$+ H_{M4}^{AC}(|m,n\rangle\langle m+1,n-2| + |m,n\rangle\langle m+1,n+2|)$$
$$+ H_{M5}^{AC}(|m,n\rangle\langle m-1,n-2| + |m,n\rangle\langle m-1,n+2|)$$
$$+ H_{M6}^{AC}(|m,n\rangle\langle m+3,n+2| + |m,n\rangle\langle m+3,n-2|)$$
$$+ H_{M7}^{AC}(|m,n\rangle\langle m-3,n+2| + |m,n\rangle\langle m-3,n-2|)$$
$$+ H_{M3}^{AC}|m,n\rangle\langle m-2,n|, \tag{D3}$$

with

$$H_{M1}^{AC} = H_M^E(\vec{C}_2)e^{ik_y\vec{C}_2.\hat{y}} + H_M^E(\vec{C}_5)e^{ik_y\vec{C}_5.\hat{y}},$$

$$H_{M2}^{AC} = H_M^E(\vec{S}_1)e^{ik_y\vec{S}_1.\hat{y}},$$

$$H_{M3}^{AC} = H_M^E(\vec{S}_4)e^{ik_y\vec{S}_4.\hat{y}},$$

$$H_{M4}^{AC} = \left[H_M^E(\vec{S}_2)e^{ik_y\vec{S}_2.\hat{y}} + H_M^E(\vec{S}_6)e^{ik_y\vec{S}_6.\hat{y}}\right],$$

$$H_{M5}^{AC} = \left[H_M^E(\vec{S}_3)e^{ik_y\vec{S}_3.\hat{y}} + H_M^E(\vec{S}_5)e^{ik_y\vec{S}_5.\hat{y}}\right],$$

$$H_{M6}^{AC} = \left[H_M^E(\vec{C}_1)e^{ik_y\vec{C}_1.\hat{y}} + H_M^E(\vec{C}_6)e^{ik_y\vec{C}_6.\hat{y}}\right],$$

$$H_{M7}^{AC} = \left[H_M^E(\vec{C}_3)e^{ik_y\vec{C}_3.\hat{y}} + H_M^E(\vec{C}_4)e^{ik_y\vec{C}_4.\hat{y}}\right], \tag{D4}$$

$$H_{X\text{-}X}^{AC}$$
$$= H_{X1}^{AC}|m,n\rangle\langle m,n| + H_{X2}^{AC}|m,n\rangle\langle m+2,n|$$
$$+ H_{X4}^{AC}(|m,n\rangle\langle m+1,n-2| + |m,n\rangle\langle m+1,n+2|)$$
$$+ H_{X5}^{AC}(|m,n\rangle\langle m-1,n-2| + |m,n\rangle\langle m-1,n+2|)$$
$$+ H_{X6}^{AC}(|m,n\rangle\langle m+3,n+2| + |m,n\rangle\langle m+3,n-2|)$$
$$+ H_{X7}^{AC}(|m,n\rangle\langle m-3,n+2| + |m,n\rangle\langle m-3,n-2|)$$
$$+ H_{X3}^{AC}|m,n\rangle\langle m-2,n|, \tag{D5}$$

with

$$H_{X1}^{AC} = H_X^E(\vec{C}_2)e^{ik_y\vec{C}_2.\hat{y}} + H_X^E(\vec{C}_5)e^{ik_y\vec{C}_5.\hat{y}},$$

$$H_{X2}^{AC} = H_X^E(\vec{S}_1)e^{ik_y\vec{S}_1.\hat{y}},$$

$$H_{X3}^{AC} = H_X^E(\vec{S}_4)e^{ik_y\vec{S}_4.\hat{y}},$$

$$H_{X4}^{AC} = H_X^E(\vec{S}_2)e^{ik_y\vec{S}_2.\hat{y}} + H_X^E(\vec{S}_6)e^{ik_y\vec{S}_6.\hat{y}},$$

$$H_{X5}^{AC} = H_X^E(\vec{S}_3)e^{ik_y\vec{S}_3.\hat{y}} + H_X^E(\vec{S}_5)e^{ik_y\vec{S}_5.\hat{y}},$$

$$H_{X6}^{AC} = H_X^E(\vec{C}_1)e^{ik_y\vec{C}_1.\hat{y}} + H_X^E(\vec{C}_6)e^{ik_y\vec{C}_6.\hat{y}},$$

$$H_{X7}^{AC} = H_X^E(\vec{C}_3)e^{ik_y\vec{C}_3.\hat{y}} + H_X^E(\vec{C}_4)e^{ik_y\vec{C}_4.\hat{y}}. \tag{D6}$$

$$H_{M\text{-}X}^{AC}$$
$$= H_{MX1}^{AC}|m,n\rangle\langle m,n-3| + H_{MX1}^{AC}|m,n\rangle\langle m,n+1|$$
$$+ H_{MX2}^{AC}|m,n\rangle\langle m-1,n-1|$$
$$+ H_{MX3}^{AC}|m,n\rangle\langle m+1,n-1|, \tag{D7}$$

$$H_{X\text{-}M}^{AC}$$
$$= H_{MX1}^{\dagger AC}|m,n\rangle\langle m,n+3| + H_{MX1}^{\dagger AC}|m,n\rangle\langle m,n-1|$$
$$+ H_{MX2}^{\dagger AC}|m,n\rangle\langle m+1,n+1|$$
$$+ H_{MX3}^{\dagger AC}|m,n\rangle\langle m-1,n+1|, \tag{D8}$$

with

$$H_{MX1}^{AC} = H_{M-X}^E(\vec{A}_1)e^{ik_y\vec{A}_1.\hat{y}},$$

$$H_{MX2}^{AC} = H_{M-X}^E(\vec{A}_2)e^{ik_y\vec{A}_2.\hat{y}},$$

$$H_{MX3}^{AC} = H_{M-X}^E(\vec{A}_3)e^{ik_y\vec{A}_3.\hat{y}}. \tag{D9}$$

The τ index and the SOC matrix are the same as those for the zigzag nanoribbon.

[1] F. C. Wu, F. Y. Qu, and A. H. MacDonald, Phys. Rev. B **91**, 075310 (2015).

[2] K. F. Mak *et al.*, Science **344**, 1489 (2014).

[3] F. Y. Qu, A. C. Dias, J. Y. Fu, L. V. Lelovsky, and D. L. Azevedos, Sci. Rep. **7**, 41044 (2016).

[4] T. Cao *et al.*, Nat. Commun. **3**, 887 (2012).

[5] D. Oliveira, J. Fu, L. Villegas-Lelovsky, A. C. Dias, and F. Qu, Phys. Rev. B **93**, 205422 (2016).

[6] D. Xiao, G.-B. Liu, W. Feng, X. Xu, and W. Yao, Phys. Rev. Lett. **108**, 196802 (2012).

[7] P. Dey, L. Y. Yang, C. Robert, G. Wang, B. Urbaszek, X. Marie, and S. A. Crooker, Phys. Rev. Lett. **119**, 137401 (2017).

[8] K. F. Mak *et al.*, Nat. Nanotechnol. **7**, 494 (2012).

[9] A. M. Jones *et al.*, Nat Nanotechnol. **8**, 634 (2013).

[10] J. Zaumseil, Science **344**, 702 (2014).

[11] V. Orsi Gordo, M. A. G. Balanta, Y. Galvao Gobato, F. S. Covre, H. V. A. Galeti, F. Iikawa, O. D. D. Couto, F. Qu, M. Henini, D. W. Hewak, and C. C. Huang, Nanoscale **10**, 4807 (2018).

[12] G. Aivazian, Z. R. Gong, A. M. Jones, R. L. Chu, J. Q. Yan, D. G. Mandrus, C. W. Zhang, D. Cobden, W. Yao, and X. D. Xu, Nat. Phys. **11**, 148 (2015).

[13] J. Fu, A. Bezerra, and F. Qu, Phys. Rev. B **97**, 115425 (2018).

[14] G. Wang, X. Marie, B. L. Liu, T. Amand, C. Robert, F. Cadiz, P. Renucci, and B. Urbaszek, Phys. Rev. Lett. **117**, 187401 (2016).

[15] K. Hao, L. Xu, F. Wu, P. Nagler, K. Tran, X. Ma, C. Schüller, T. Korn, A. H MacDonald, G. Moody, and X. Li, 2D Mater. **4**, 025105 (2017).

[16] K. Hao, G. Moody, F. Wu, C. K. Dass, L. Xu, C.-H. Chen, L. Sun, M.-Y. Li, L.-J. Li, A. H. MacDonald, and X. Li, Nat. Phys. **12**, 677 (2016).

[17] Z. L. Ye, D. Z. Sun, and T. F. Heinz, Nat. Phys. **13**, 26 (2017).

[18] P. Giannozzi *et al.*, J. Phys.: Condens. Matter **21**, 395502 (2009).

[19] J. Clark Stewart *et al.*, "zkri", 2005, First principles methods using CASTEP.

[20] J. A. Silva-Guillén, P. San-Jose, and R. Roldán, Appl. Sci. **6**, 284 (2016).

[21] G.-B. Liu, W.-Y. Shan, Y. Yao, W. Yao, and D. Xiao, Phys. Rev. B **88**, 085433 (2013).

[22] H. Rostami, R. Roldán, E. Cappelluti, R. Asgari, and F. Guinea, Phys. Rev. B **92**, 195402 (2015).

[23] E. Cappelluti, R. Roldán, J. A. Silva-Guillén, P. Ordejón, and F. Guinea, Phys. Rev. B **88**, 075409 (2013).

[24] S. Fang, R. Kuate Defo, S. N. Shirodkar, S. Lieu, G. A. Tritsaris, and E. Kaxiras, Phys. Rev. B **92**, 205108 (2015).

[25] E. Ridolfi, D. Le, T. S. Rahman, E. R. Mucciolo, and C. H. Lewenkopf, J. Phys.: Condens. Matter **27**, 365501 (2015).

[26] F. Zahid, L. Liu, Y. Zhu, J. Wang, and H. Guo, AIP Adv. **3**, 052111 (2013).

[27] H. Rostami, A. G. Moghaddam, and R. Asgari, Phys. Rev. B **88**, 085440 (2013).

[28] S. Pavlović and F. M. Peeters, Phys. Rev. B **91**, 155410 (2015).

[29] S. Fang, S. Carr, J. Y. Shen, M. A. Cazalilla, and E. Kaxiras, arXiv:1709.07510.

[30] J.-B. Wu, H. Zhao, Y. Li, D. Ohlberg, W. Shi, W. Wu, H. Wang, and P.-H. Tan, Adv. Opt. Mater. **4**, 756 (2016).

[31] Y. Y. Chen, P. Cui, X. B. Ren, C. D. Zhang, C. H. Jin, Z. Y. Zhang, and C. K. Shih, Nat. Commun. **8**, 15135 (2017).

[32] F. Cheng, H. Xu, W. Xu, P. Zhou, J. Martin, and K. P. Loh, Nano Lett. **17**, 1116 (2017).

[33] W. J. Schutte, J. L. De Boer, and F. Jellinek, J. Solid State Chem. **70**, 207 (1987).

[34] D. Puotinen and R. E. Newnham, Acta Crystallogr. **14**, 691 (1961).

[35] P. B. James and M. T. Lavik, Acta Crystallogr. **16**, 1183 (1963).

[36] R. W. G. Wyckoff, *Crystal Structures*, Vol. 1 (Wiley, New York, 1963).

[37] J. P. Perdew, K. Burke, and M. Ernzerhof, Phys. Rev. Lett. **77**, 3865 (1996).

[38] C.-Y. Luan, S. Xie, C. Ma, S. Wang, Y. Kong, and M. Xu, Appl. Phys. Lett. **111**, 073105 (2017).

[39] H. Rostami, R. Asgari, and F. Guinea, J. Phys.: Condens. Matter **28**, 495001 (2016).

[40] A. R. Botello-Méndez, F. López-Urías, M. Terrones, and H. Terrones, Nanotechnology **20**, 325703 (2009).

[41] R. Roldán, M. P. López-Sancho, F. Guinea, E. Cappelluti, J. A. Silva-Guillén, and P. Ordejn, 2D Mater. **1**, 034003 (2014).

[42] A. C. Dias, J. Y. Fu, L. V. Lelovsky, and F. Y. Qu, J. Phys.: Condens. Matter **28**, 375803 (2016).

[43] N. Salami and A. A. Shokri, J. Phys. Chem. Solids **90**, 16 (2016).

[44] R.-L. Chu, G.-B. Liu, W. Yao, X. Xu, D. Xiao, and C. Zhang, Phys. Rev. B **89**, 155317 (2014).

[45] M. R. Guassi, G. S. Diniz, N. Sandler, and F. Qu, Phys. Rev. B **92**, 075426 (2015).

[46] F. Qu, L. Villegas-Lelovsky, and G. S. Diniz, Phys. Status Solidi, Rapid Res. Lett. **10**, 409 (2015).

[47] R. Wang, X. Y. Zhou, X. Y. Xu, J. G. Hu, and J. Pan, J. Phys. D: Appl. Phys. **50**, 095102 (2017).

[48] F. P. Ouyang, Z. X. Yang, X. Ni, N. N. Wu, Y. Chen, and X. Xiong, Appl. Phys. Lett. **104**, 071901 (2014).

[49] C. Chen, X. F. Wang, Y. S. Li, X. M. Cheng, and A. L. Yao, J. Phys. D: Appl. Phys. **50**, 465302 (2017).